SITE CHARACTERIZATION REPORT
SDAK: Davos (GR) - Kongresszentrum

Manuel Hobiger, Clotaire Michel, Jan Burjánek, Donat Fäh

Last Modification: 22nd April, 2016

Contents

1 Summary

The old station SDAS in Davos was replaced by the modern free-field SSMNet station SDAK close to the Congress Centre in the center of Davos. We performed two passive seismic arrays for the site characterization, a smaller one next to the station and a large one in the Kurpark. The site characterization measurements showed that the fundamental frequency of the structure beneath the station is about 1.5 Hz. The polarization analysis showed a two-dimensional polarization of the valley at a frequency of 1.1 Hz in the Kurpark, i.e. at a lower frequency than the ellipticity peak. This observed 2-dimensional polarization cannot be well explained by the other measurements we made and was not further considered for the inversion.

The array measurements were analyzed with three different techniques, namely 3-component HRFK, WaveDec and SPAC. All techniques gave coincident dispersion curves. The fundamental mode Love and Rayleigh wave dispersion curves could be retrieved at both arrays. In the Kurpark, the first higher mode of each wave could be observed as well. Joint inversions of dispersion and ellipticity curves yielded principally a model with two layers over the seismic bedrock. The upper layers consist of alluvial sands and gravels, the seismic bedrock of moraine. The bedrock depth is around 60 m in the Kurpark and around 47 m next to station SDAK. The V_{S30} value there is around 275 m/s.

2 Introduction

In the framework of the second phase of the Swiss Strong Motion Network (SSMNet) renewal project, a renewal of the old seismic station SDAS in Davos was decided. Station SDAS (Davos - Am Stein) was operational between 1992 August 25 and 2003 August 1. It was located in a transformator house on a steep hill close to the center of Davos (see 1). A replacement at the location of the old station was not possible because there was no suitable space in the vicinity of the transformator house due to the steepness of the area. Consequently, a new location had to be found. An H/V survey and ensuing test measurements at three possible sites resulted in the selection of the Congress Centre as the best location for the new station SDAK. The new station went operational on 17 March 2015.
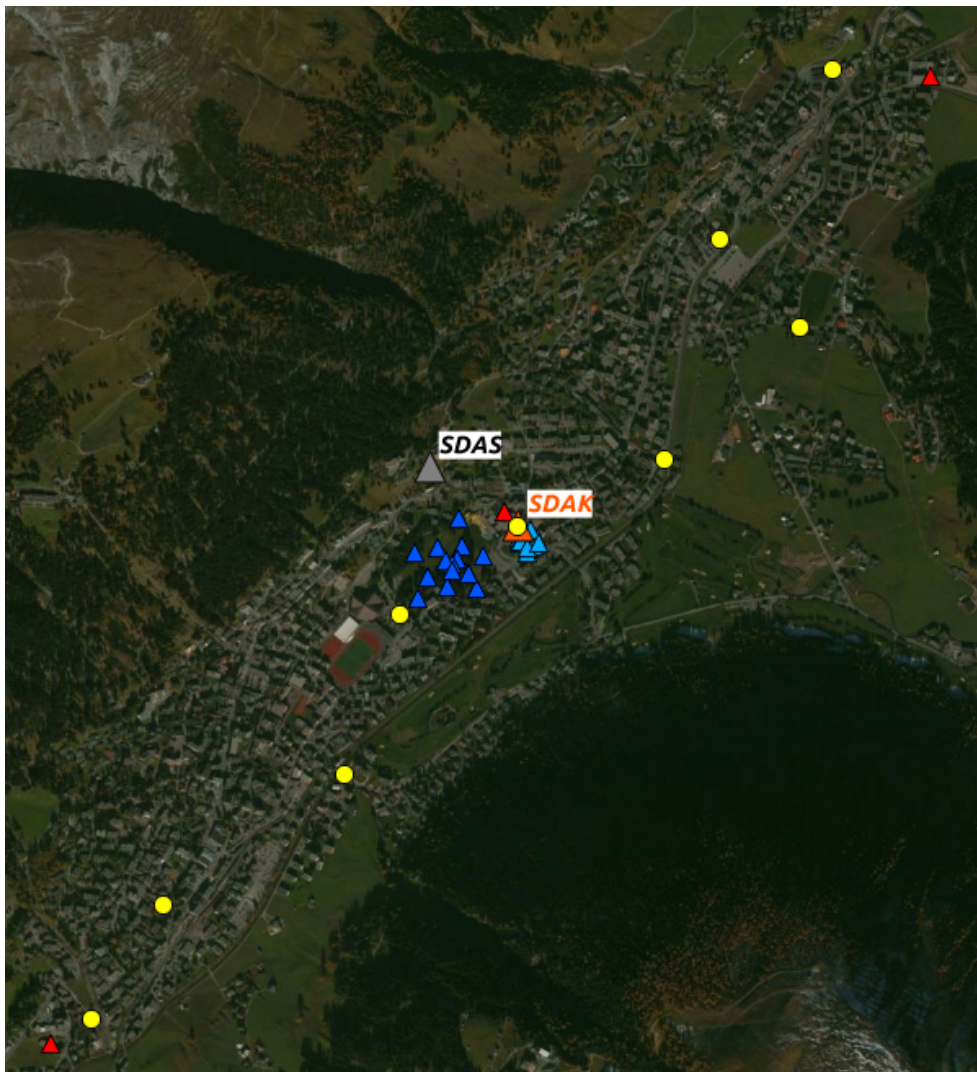
Figure 1: Map of Davos showing the different stations and measurements performed. SDAS was a station of the old SSMNet and operational until August 2013. The new station SDAK is located next to the Congress Centre. The yellow circles represent the locations of the H/V test measurements. The red triangles are the places where test installations longer than a week were performed. The light and dark blue triangles are the station locations of the final passive site characterization array measurements.

3   Site selection

3.1   H/V test measurements

In order to investigate the variability of the soil structure in Davos and to identify interesting sites for the implementation of the new seismic station, an H/V survey was performed. Fig. 2 shows the locations of the H/V points and the measured fundamental frequencies. The corresponding H/V curves are shown in Fig. 3.

All H/V points were measured in the sedimentary basin of the Landwasser river and show clear H/V peaks. Test measurements in the northeast show relatively high fundamental frequencies of up to 9.2 Hz. There is a general trend of decreasing fundamental frequencies to the southwest, indicating thicker sedimentary layers to the southwest. At the last point to the southwest, the fundamental frequency is only 0.56 Hz. Station DAV05, which is closest to the final site location, shows a relatively broad H/V peak at 1.4 Hz, which is quite representative for most of the center of Davos.
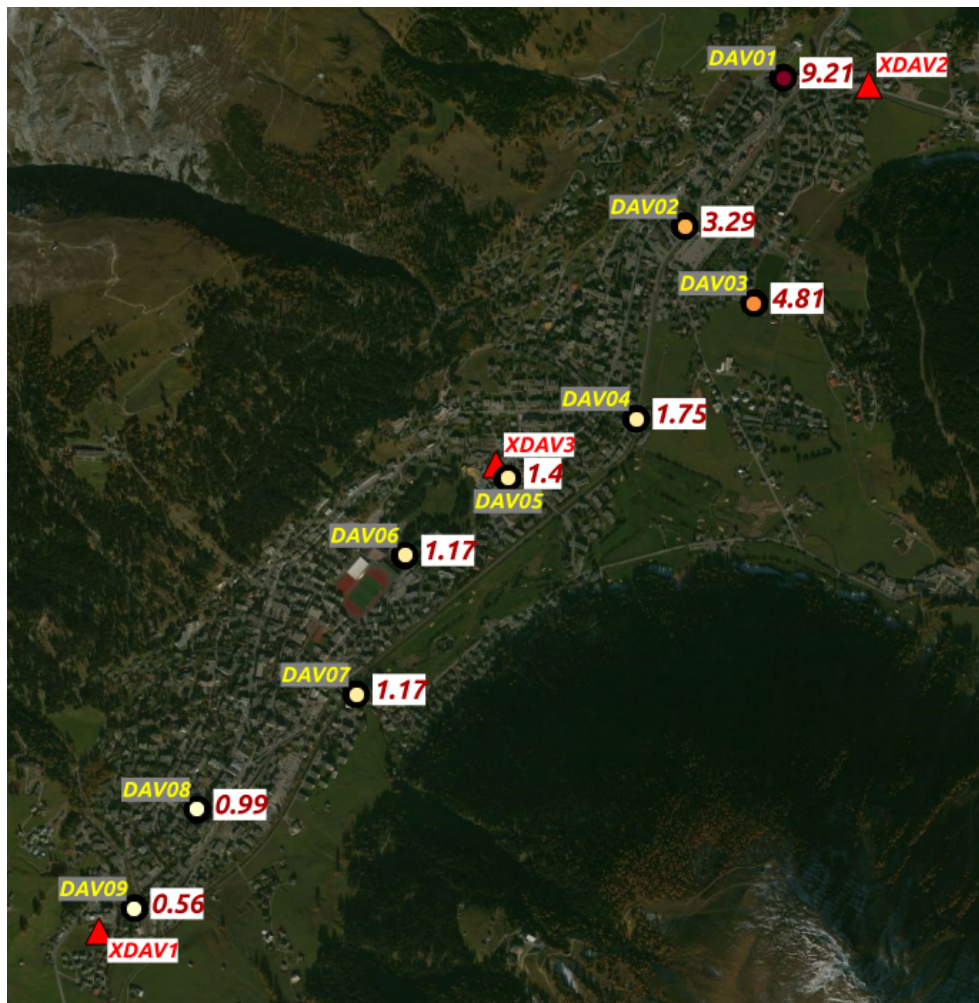

Figure 2: Map of the locations of the H/V measurement points (yellow labels) and the measured fundamental frequencies (red numbers). The red triangles are the places where test installations longer than a week were performed.
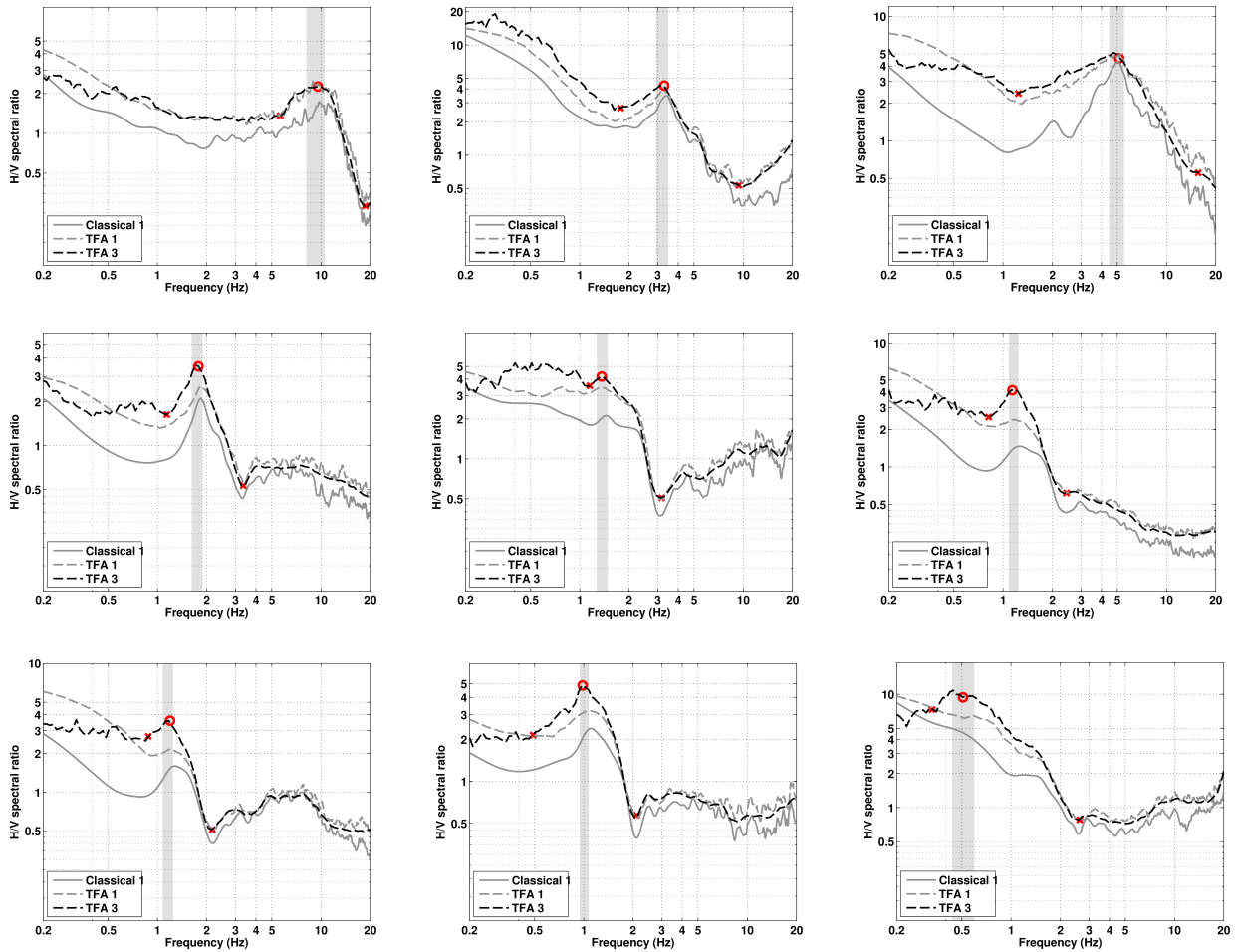
Figure 3: Ellipticity curves for the measurement points shown in Fig. 2 for points DAV01, DAV02, DAV03 (first line), DAV04, DAV05, DAV06 (center line) and finally DAV07, DAV08 and DAV09 (bottom line). The solid grey lines correspond to the results of the classical H/V ratio, calculated with geopsy. The dashed grey lines correspond to the time-frequency analysis code of Fäh et al. (2001), the dashed grey lines to the time-frequency analysis code of Fäh et al. (2009). The latter are used as reference.

3.2 Noise test measurements

In total, three possible installation sites have been selected for test measurements of more than a week:

- Spital Davos (XDAV1)

- WSL-Institut für Schnee- und Lawinenforschung SLF (XDAV2)

- Congress Centre Davos (XDAV3)

The locations of these sites are also indicated in Fig. 2. The data of these long-term measurements were analyzed using the PQLX method (McNamara and Buland, 2004). The results are displayed in Fig. 4. The figures show the histogram distribution of the noise level at the test installations for different frequencies.

All test stations have an acceptable noise level. At the SLF site, there was no space available to construct the station. Finally, the location at the Congress Centre was chosen because it is the most representative for Davos.
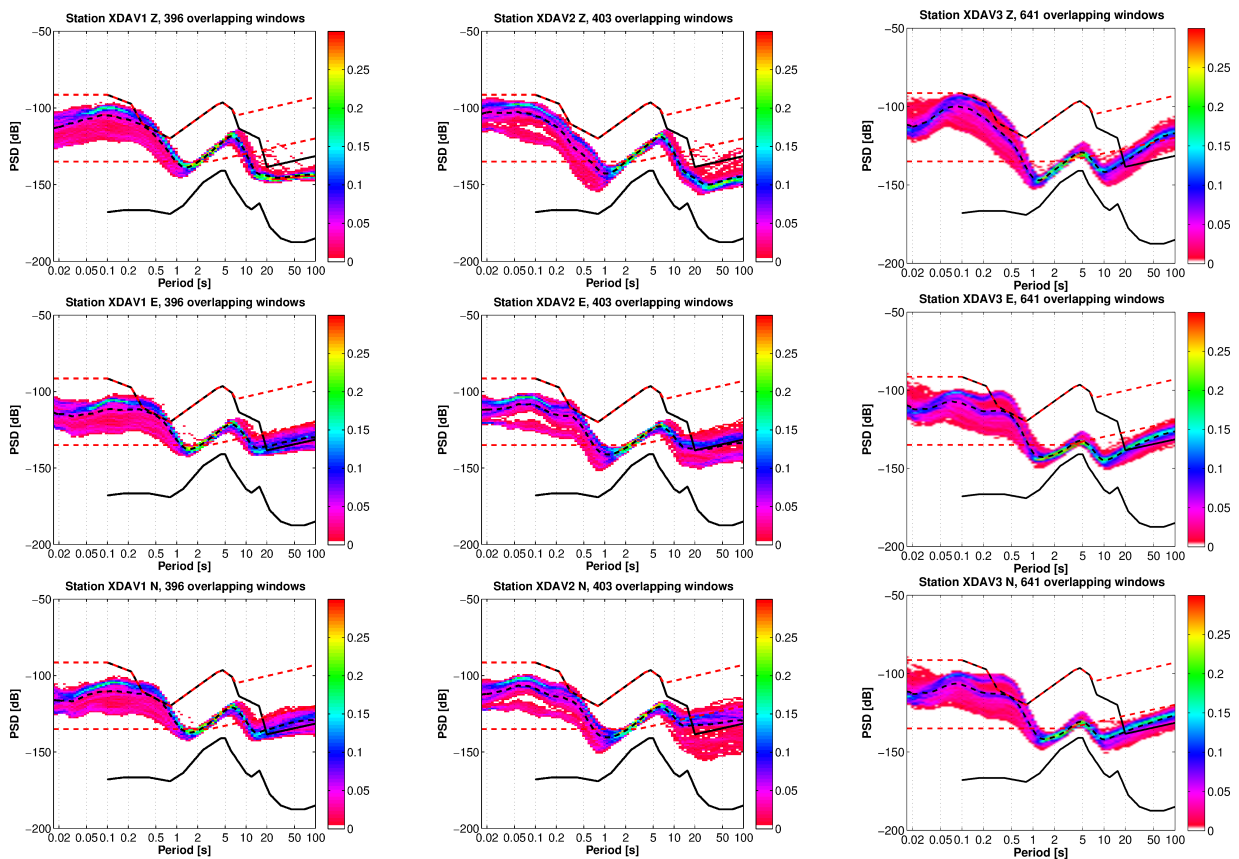

Figure 4: PQLX results on the vertical component (top line), the eastern component (central line) and the northern component (bottom line) for the test measurements at the Spital (left), the SLF (center) and the Congress Centre (right). The solid black lines correspond to world-wide high- and low-noise levels.
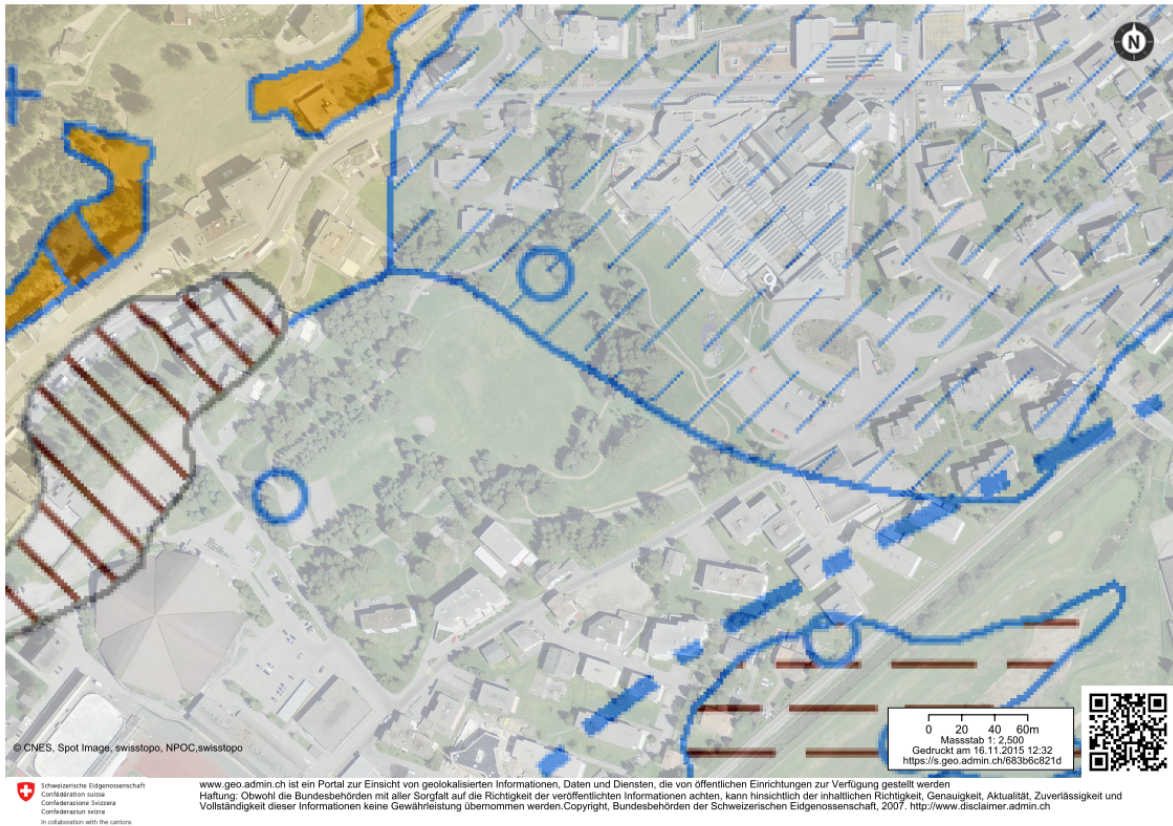
8

4   Geological setting

Figure 5: Geological map of Davos with transparent aerial image. The area around the Congress Centre, where the station is located, consists of creek debris, the area around the Kurpark consists of alluvial deposits.

For the central area of Davos around station SDAK, many geological information are available. In the Swiss geological atlas (Fig. 5), the underground under the seismic station consists of creek debris, the area in the Kurpark of alluvial deposits. However, the difference between both geologies does not seem very pronounced.

In the framework of a project to use geothermal water for the heating of the Congress Centre, different measurements were carried out in the Kurpark by Geotest. First, a seismic profile crossing the Kurpark was laid out and measured (Regli et al., 2010). The result of this measurement is shown in Fig. 6. The Kurpark is in the left part of the flat area in the profile, approximately between the station numbers 350 and 450. This seismic profile indicates the presence of a sedimentary basin of about 100 m thickness above the bedrock.

A second measurement consisted of the drilling of a borehole of 400 m depth in the Kurpark (Regli et al., 2013). The location of this borehole is indicated in Fig. 8. The resulting geological profile is shown in Fig. 7. The geology in the Kurpark consists of a first layer of gravel of several meters thickness, followed by lacustrine sand and gravel deposits which reach a depth of around 60 m. Below that, a moraine layer follows. Finally, the geological bedrock is formed by triassic dolomite at depths below 100 m.
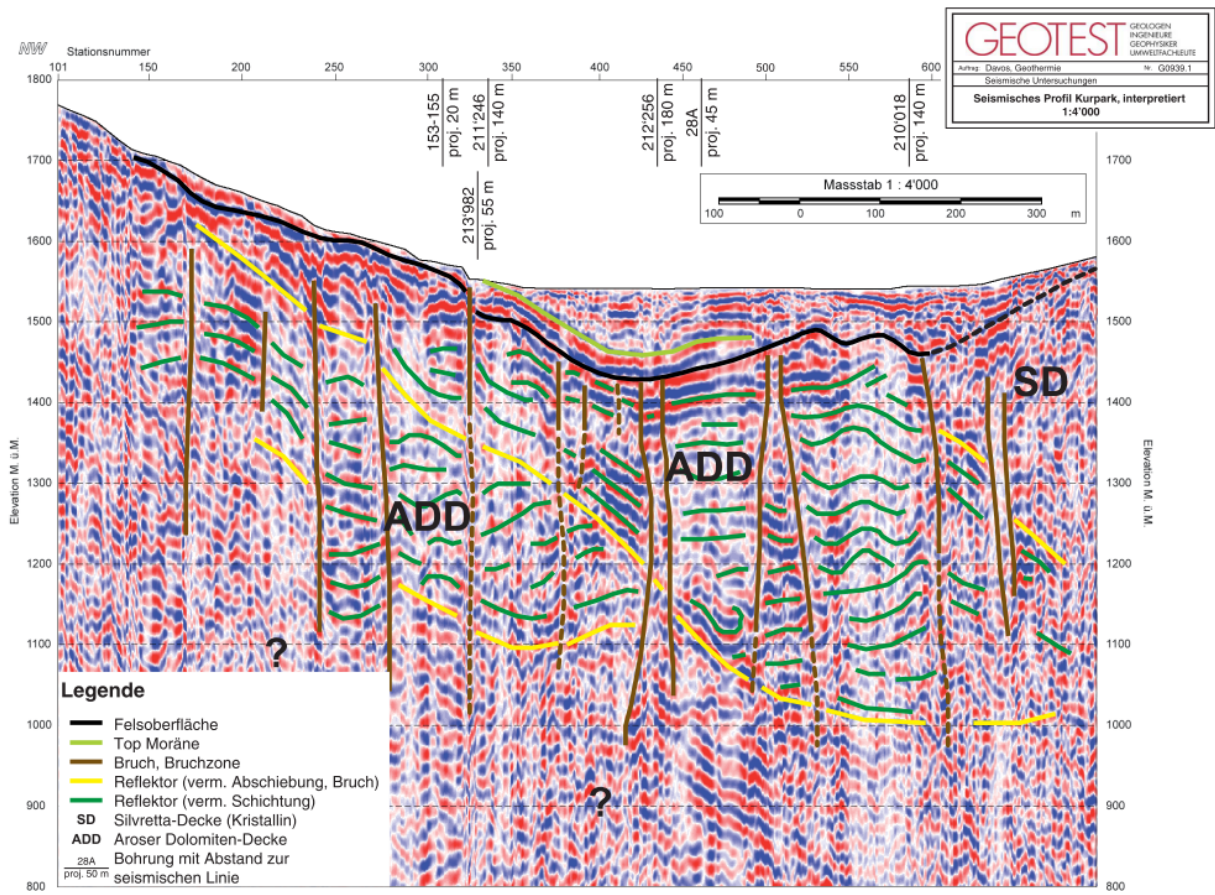
Figure 6: Seismic profile measured across the Kurpark.

Tiefe (m)	System/Stufe	Formation/Schicht	Lithologie		Beschreibung	Hydrogeologie
	Quartär	Deckschicht		Locker-gestein	Kies	05.05.12
		Delta- und Seeablagerungen			Sand	
20						
40						
					Kies	
60					Sand	
		Moräne			Steine, Blöcke	
80					Kies	
					Sand	
					Steine, Blöcke	
100					Kies	
	Trias	Aroser Dolomit		Dolomit	schwarz, wenig Calcit	27.06.12
120						Arteser: OKT 1350 l/min
140					dunkelgrau, wenig Calcit	Wasser
					dunkelgrau bis schwarz, wenig Calcit	
160						viel Wasser
180						Wasser
200						viel Wasser
220					dunkelgrau bis grau, reichlich Calcit	Wasser
240						sehr viel Wasser
260						viel Wasser
280					grau, reichlich Calcit	sehr wenig Wasser
300						
320						
340						
360					grau, wenig Calcit, tonig	sehr wenig Wasser
380						sehr wenig Wasser
402						

Figure 7: Geological borehole profile measured in the Kurpark.

5 Site characterization

5.1 Measurements and data set

We investigated the local underground structure around station SDAK by passive seismic array measurements which took place on 2014 October 14, i.e. at a time where SDAK was not installed yet, but the final location was already fixed. The layout of the seismic arrays is shown in Fig. 8. As the site of the station is surrounded by the Congress Centre on two sides and the available space is limited in the other directions, a smaller array (KON) of twelve stations was installed first, with the station lying on the edge of the array. The station names for this array are DAVKON followed by a two-digit number. Station DAVKON03 of this array is closest to the final location of station SDAK. It serves therefore as a reference for the measurements.

In order to measure also longer wavelengths and consequently analyze deeper layers of the sediments, a second array (KUR) was set up in the Kurpark west of the Congress Centre. The station names of this array are DAVKUR followed by a two-digit number. The parameters of both arrays are given in Table 1. The second array was planned to consist of 14 stations in total, but station DAVKUR03 was not working due to cabling problems. The array therefore finally consisted of 13 stations.

The station locations have been measured by a differential GPS system (Leica Viva GS10) and post-processed using the data of the swipos reference station DAV2, which is located 1.66 km to the northeast of station SDAK. After the post-processing, the precision of the localization for most stations was smaller than 5 cm. The localization error was larger for station DAVKON03 only, where a precision of 11 cm was achieved.

Table 1: List of the seismic array measurements in Davos.

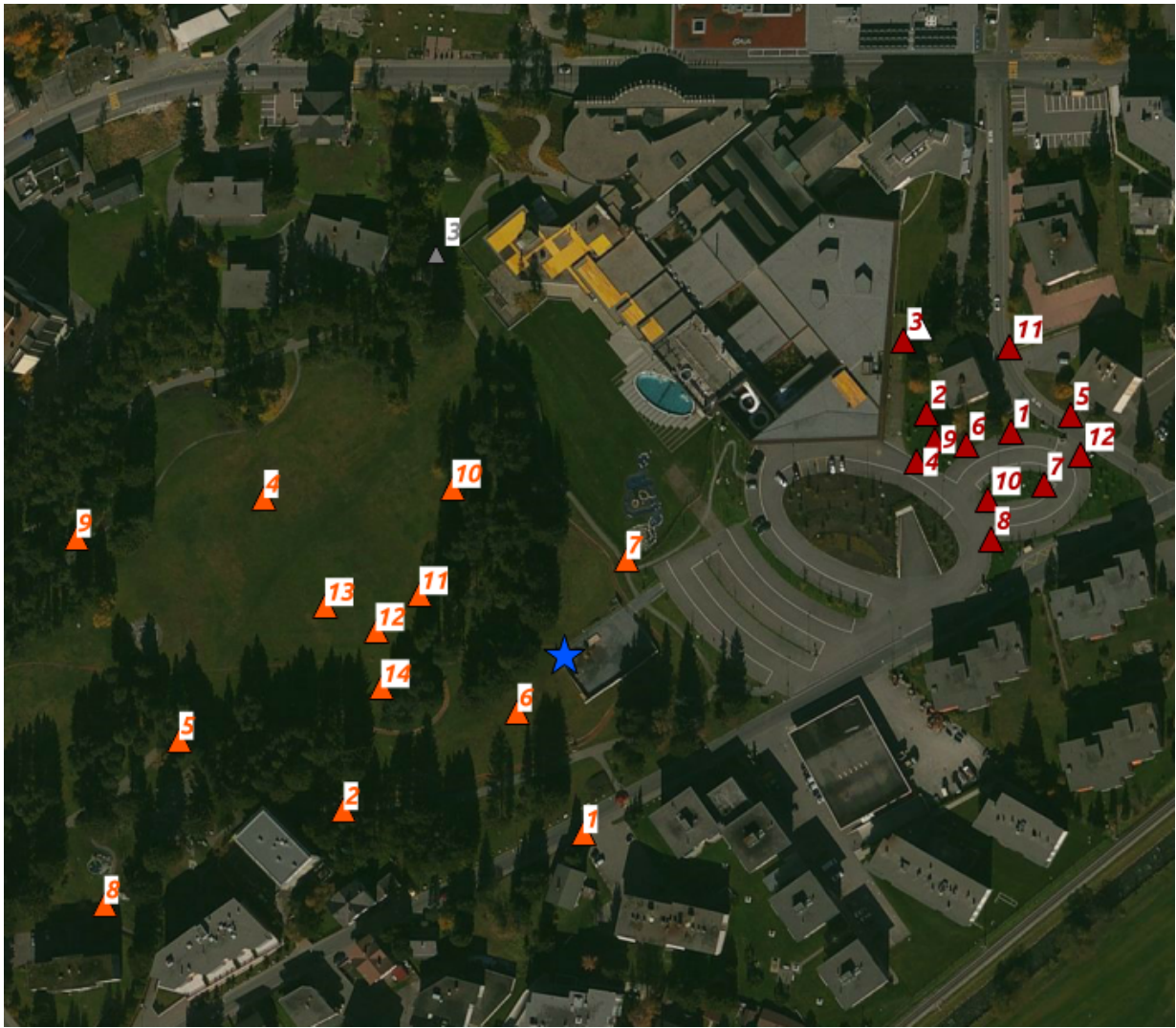| Array name	Number of sensors	Minimum interstation distance [m]	Maximum interstation distance [m]	Recording time [s]
KON	12	9.6	76.3	7200
KUR	13	19.8	219.9	7200

Figure 8: Layout of the array measurements around station SDAK. The location of SDAK is indicated by the white triangle next to station 2 of the KON array, the locations of the stations during the first array (KON) measurement by red triangles and during the second array measurement (KUR) by orange triangles. The station names for the KON (or KUR, respectively) array are DAVKON (or DAVKUR) followed by the respective two-digit number of the map. For the sake of clarity, the stations are only indicated by the respective station number. The gray station 3 belonged to the second array, but it did not record due to cabling problems. The location of the borehole is indicated by the blue star.

5.2 Measurement results

5.2.1 H/V curves

Figure 9 shows the H/V curves determined with the time-frequency analysis method (Fäh et al., 2009) for all stations of the KON and KUR arrays. In the KON array, all stations are similar and show a clear peak. The peak frequencies of the different stations range from 1.36 to 1.48 Hz. For station DAVKON03, which is closest to the location of SDAK, a peak frequency of 1.48 Hz was picked.

In the KUR array, there is more scattering in the H/V curves. Most of the stations have peak frequencies between 1.21 and 1.49 Hz, but there are three outliers with slightly larger frequencies of 1.73 Hz (DAVKUR10), 1.81 Hz (DAVKUR04) and even 2.37 Hz (DAVKUR09). These three stations are the most northerly located ones in the array. This is consistent with a decrease of the thickness of the sedimentary layers to the north of the area.
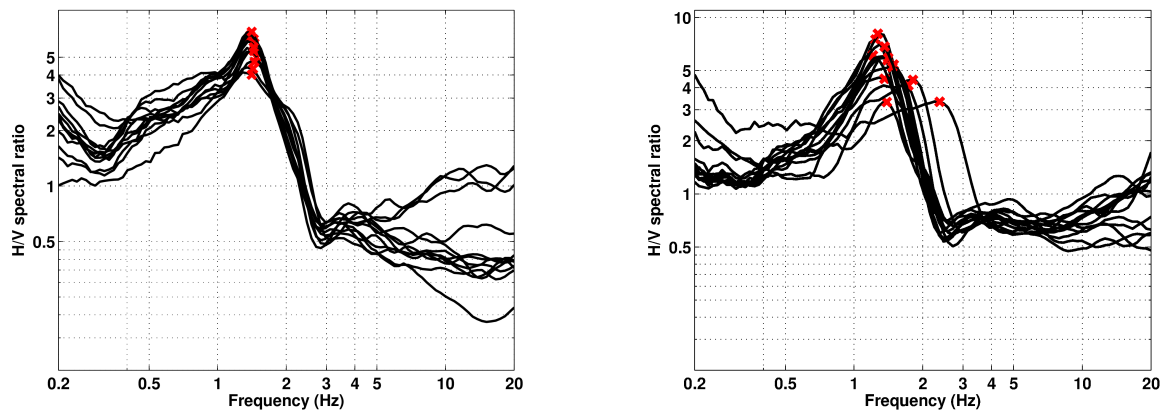

Figure 9: Overview of the H/V measurements for the different stations of the KON array measurement (left) and the KUR array measurement (right).

5.2.2 RayDec ellipticity curves

The RayDec technique (Hobiger et al., 2009) is meant to eliminate the contributions of other wave types than Rayleigh waves and give a better estimate of the ellipticity than the classical H/V technique. The RayDec ellipticity curves for all stations of the array measurements are shown in Fig. 10.

For the stations of the KON array, all stations have a clear peak at 1.48 Hz. For station DAVKON03, next to station SDAK, however, this peak is less pronounced than for the other stations. DAVKON03 shows a more pronounced peak at 2.3 Hz, followed by a strongly sloping right flank. The trough frequencies of all stations are coincident around 2.8 Hz. For station DAVKON03, the trough frequency is slightly shifted to a higher frequency of around 3.0 Hz. For higher frequencies, the curves of all stations differ a lot. Station DAVKON03 shows a secondary peak at 44 Hz.

For the KUR array, the RayDec ellipticities are more scattered. Most stations have the fundamental peak around 1.3 to 1.6 Hz. The trough frequency is around 2.5 Hz for all stations. Here again, the different curves differ a lot above the trough frequency. Station DAVKUR12 in the center of the array also shows a secondary peak at 40 Hz.
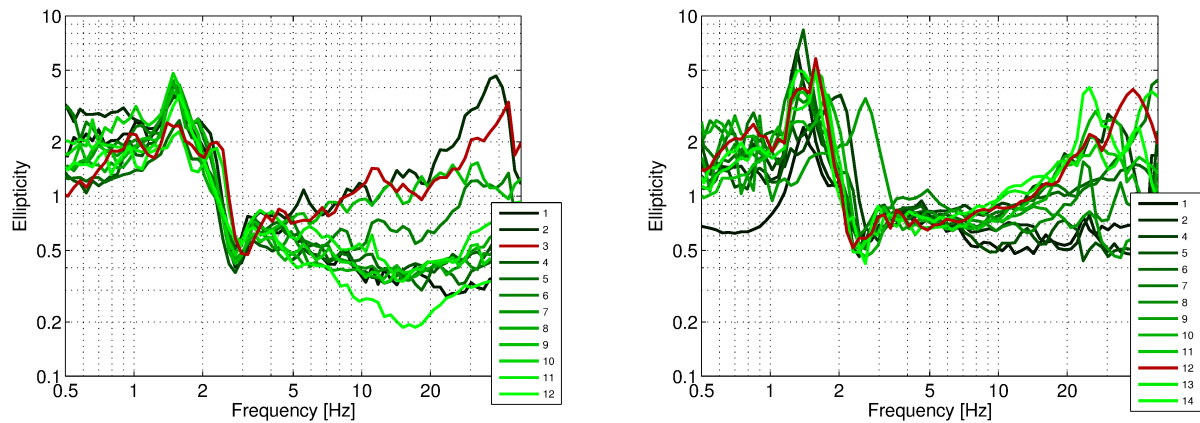

Figure 10: RayDec ellipticities for the KON array (left) and the KUR array (right).

5.2.3 Polarization measurements

The polarization parameters of the seismic noise recordings of all stations of the KON and KUR arrays are shown in Figs 11-15. An overview of the peak frequencies for all stations is given in Fig. 16. The analysis was performed according to Burjánek et al. (2010) and Burjánek et al. (2012).

For the KON array, the figures show a polarized particle motion at the stations around 1.25 Hz (the minima range from 1.21 to 1.30 Hz for the different stations), i.e. at a lower frequency than the fundamental frequency of the Rayleigh wave ellipticity curves. At this frequency, the particle motion occurs completely in the axis of the Landwasser valley. This can be interpreted as the 2-dimensional valley motion.

In the KUR array, the frequency of maximal polarization is lower and ranges from 1.06 to 1.17 Hz for the different stations, with the exception of station DAVKUR01, where the polarization is less pronounced and at a higher frequency of 1.45 Hz. This station was located close to a road with a lot of traffic, which might have influenced the result.

Stations DAVKUR04 and DAVKUR09 showed larger resonance frequencies in the H/V and ellipticity curves, but their polarization frequency coincides with the other stations, which is a strong indication for a two-dimensional valley resonance affecting all stations. For these two stations, however, the polarization is also higher for larger frequencies compared with the other stations.

For all stations, the observed polarization occurs at lower frequencies than the fundamental Rayleigh wave frequency.
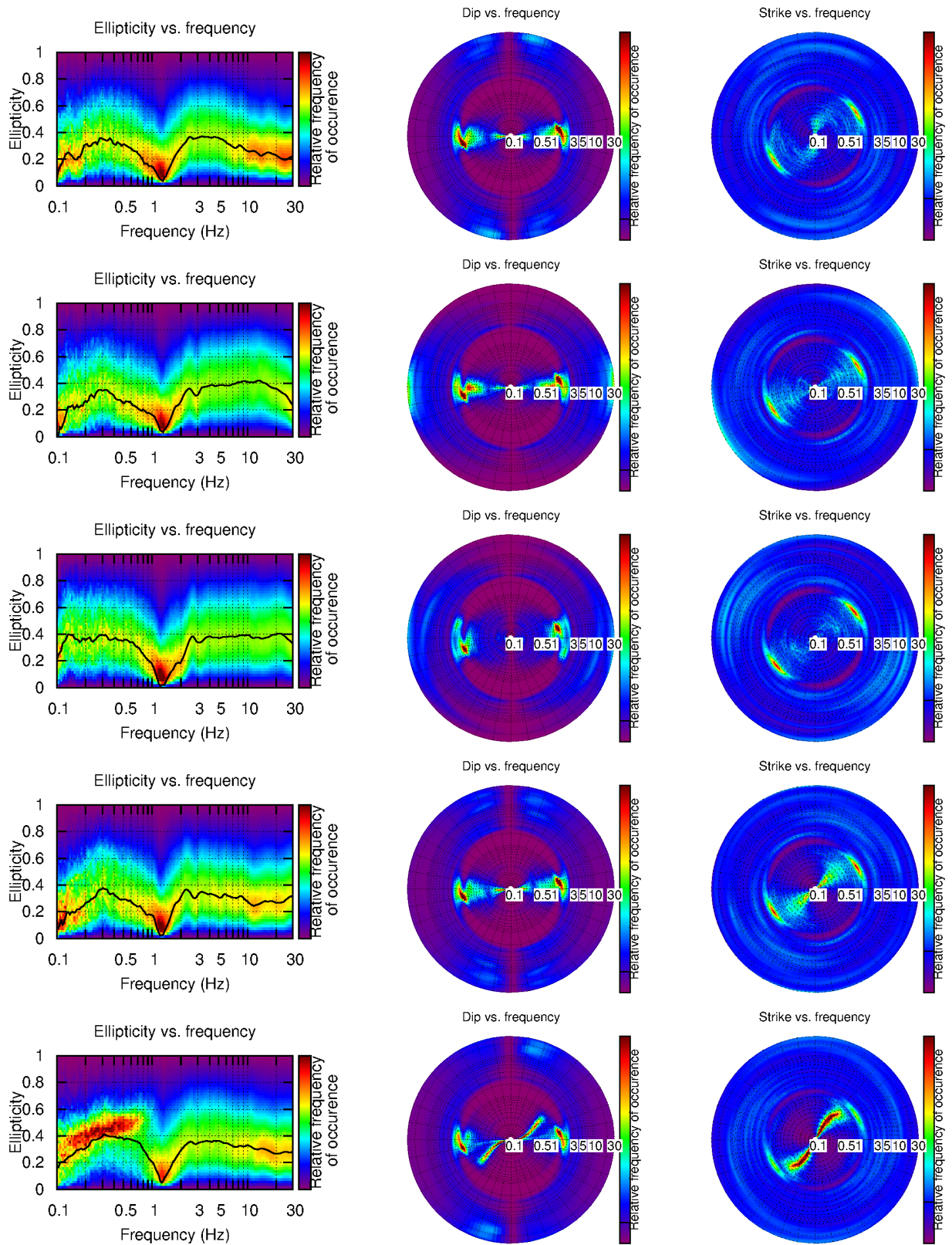
Figure 11: Polarization analysis of stations DAVKON01, DAVKON02, DAVKON03, DAVKON04 and DAVKON05 (from top to bottom).
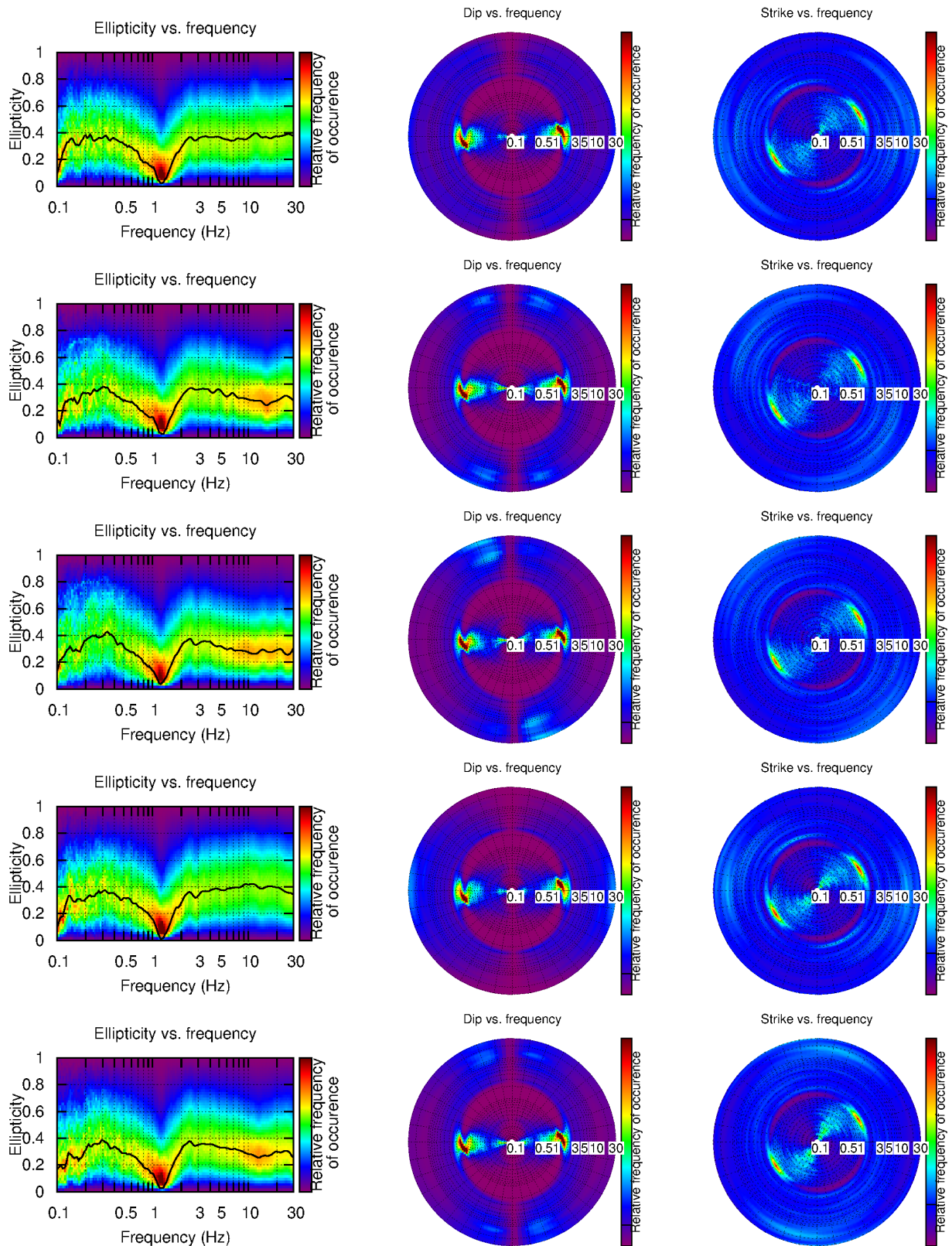
Figure 12: Polarization analysis of stations DAVKON06, DAVKON07, DAVKON08, DAVKON09 and DAVKON10 (from top to bottom).
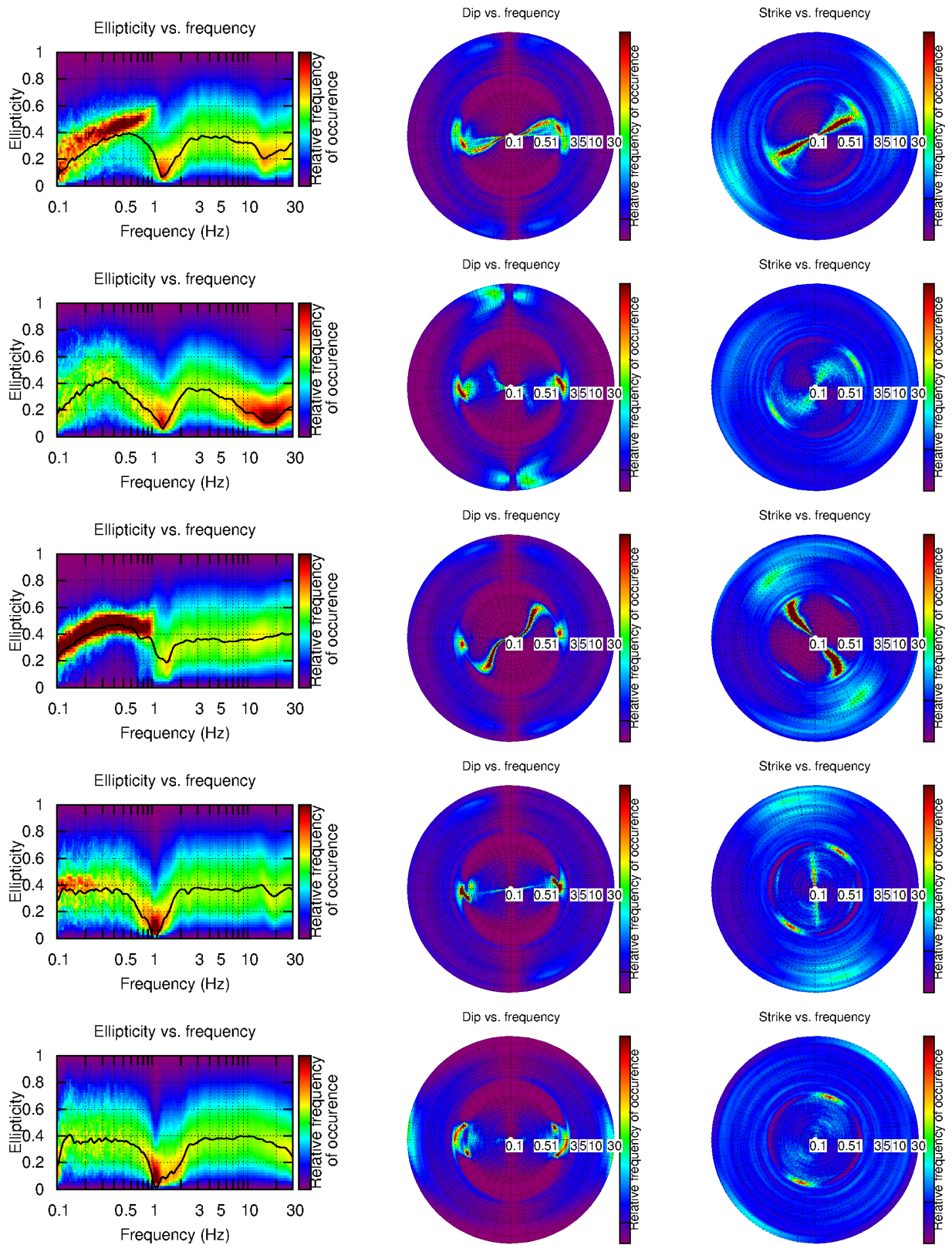
Figure 13: Polarization analysis of stations DAVKON11, DAVKON12, DAVKUR01, DAVKUR02 and DAVKUR04 (from top to bottom).
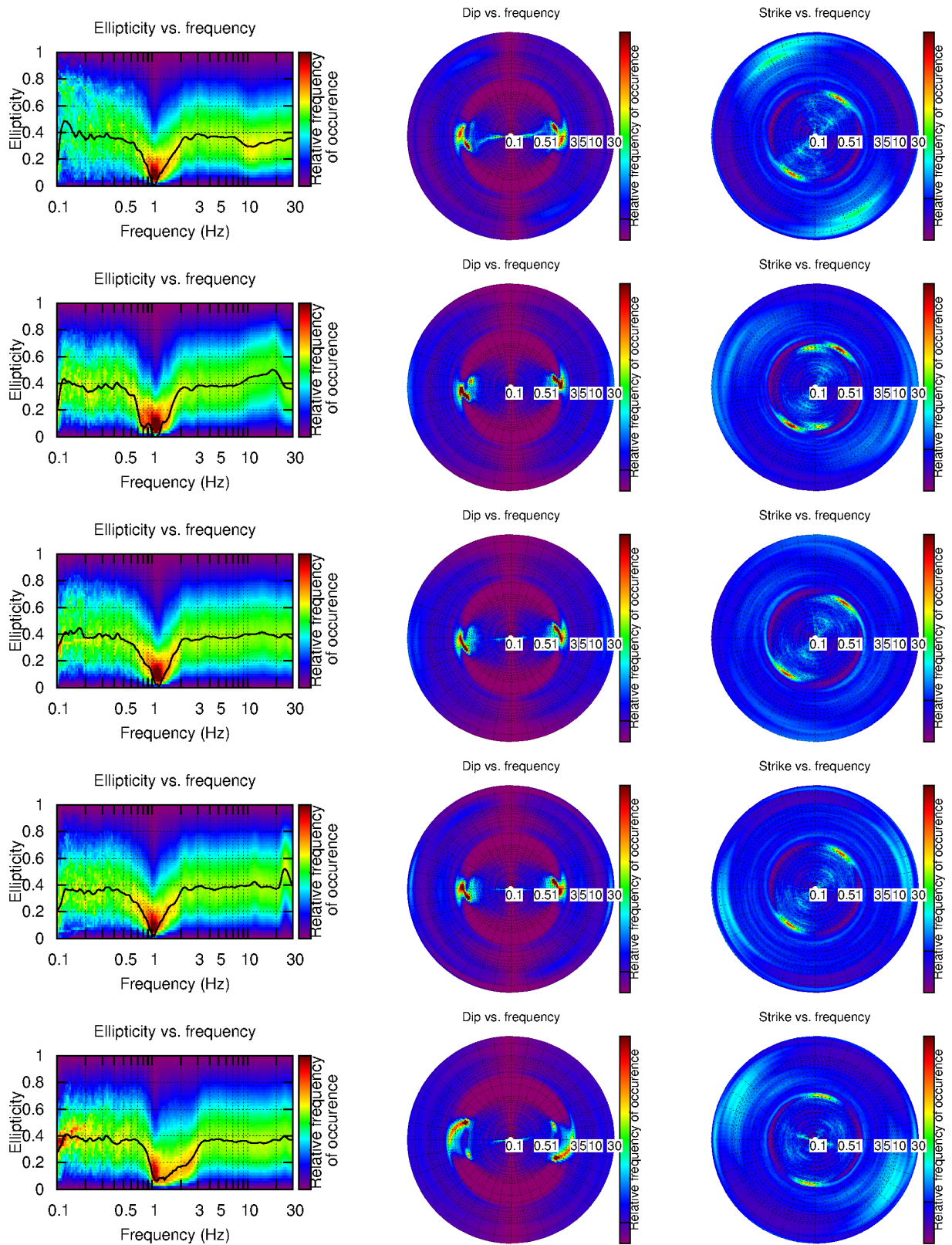
Figure 14: Polarization analysis of stations DAVKUR05, DAVKUR06, DAVKUR07, DAVKUR08 and DAVKUR09 (from top to bottom).
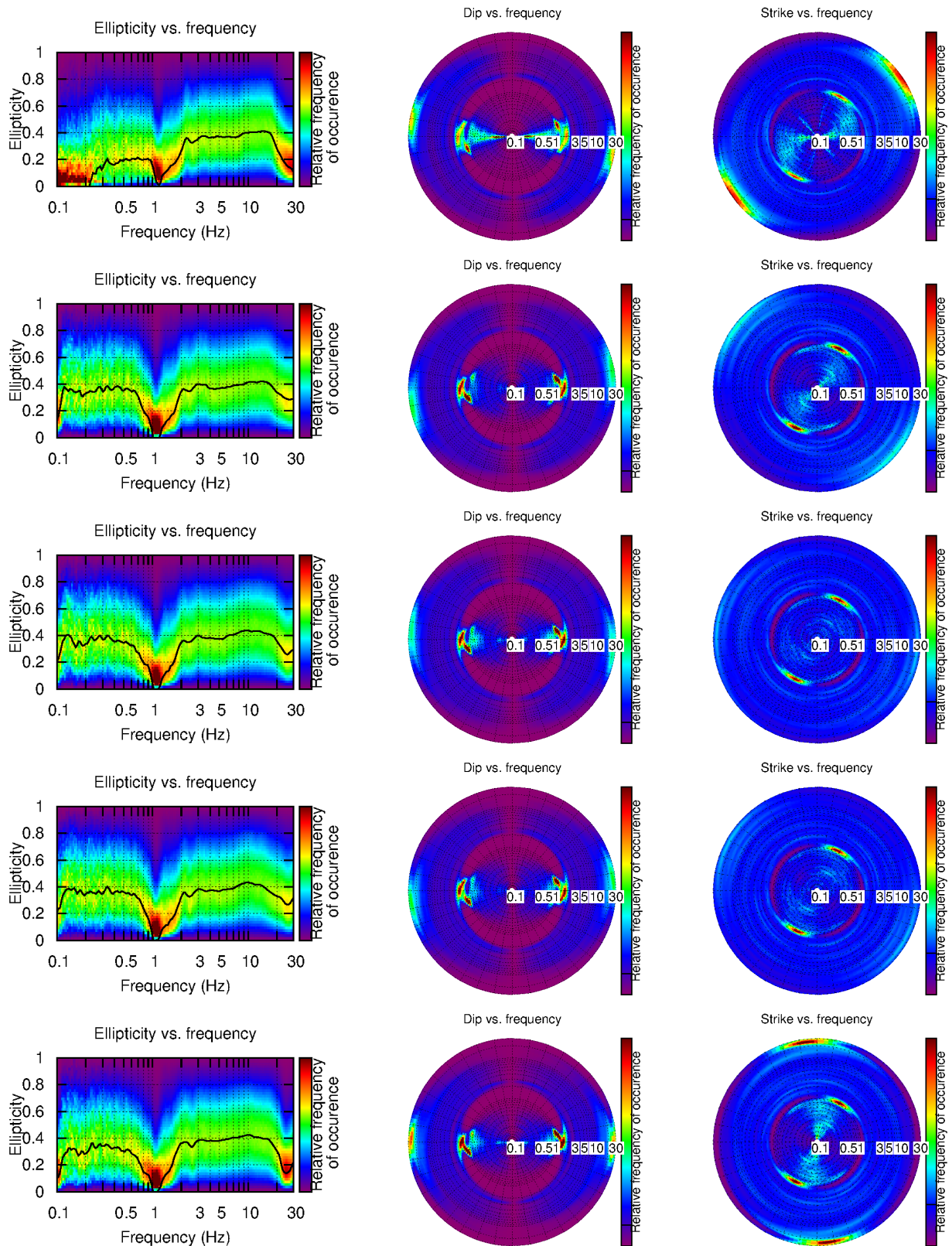
20

Figure 15: Polarization analysis of stations DAVKUR10, DAVKUR11, DAVKUR12, DAVKUR13 and DAVKUR14 (from top to bottom).
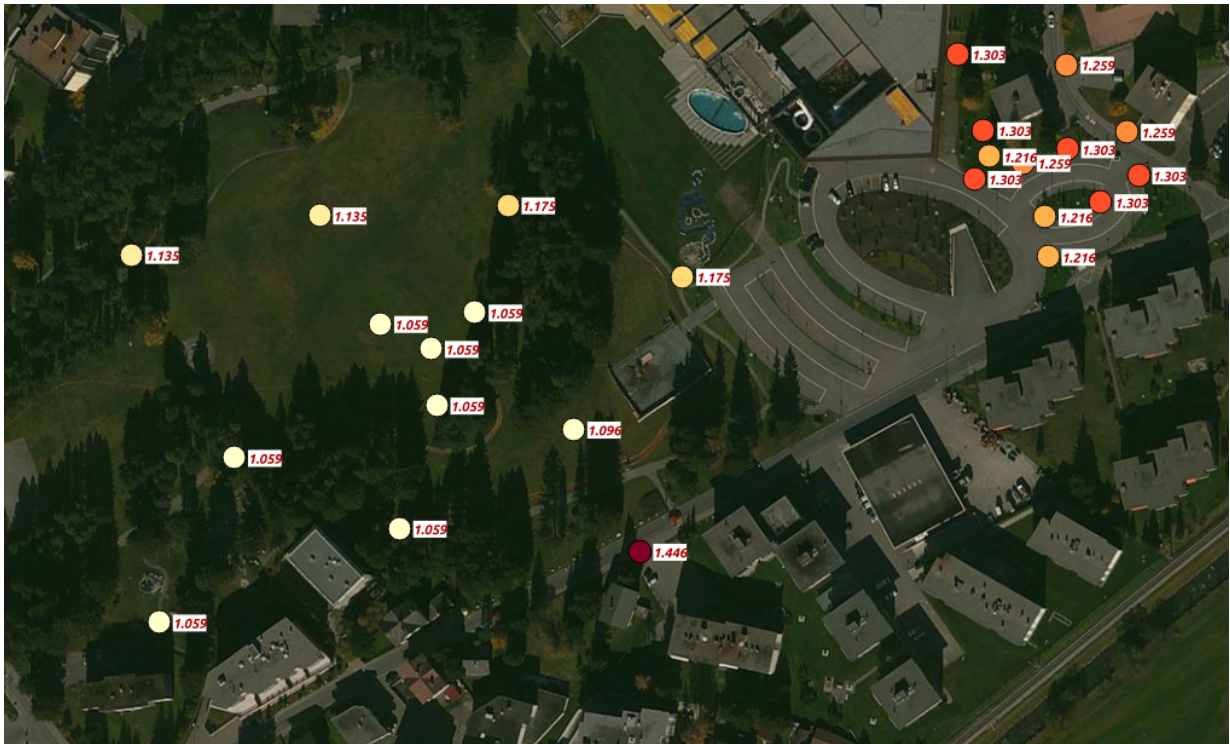
Figure 16: Map showing the peak frequencies of the linear polarization for all measurement stations.

5.3 Possible 2-dimensional valley polarization

The similar polarization pattern of the different stations indicates the possibility of a 2-dimensional valley motion. According to Bard and Bouchon (1985), the fundamental mode of the transverse (or SH) resonance of a valley is approximately given by

$$f = \frac{v_S}{4h}\sqrt{1 + \left(\frac{2h}{w}\right)^2}, \tag{1}$$

where v_S is the average shear-wave velocity in the sediments, h the thickness of the sediments and w the half-width of the sedimentary basin, i.e. the width over which the sedimentary filling is more than half of the maximum thickness deep.
From the seismic profile across the Kurpark (Fig. 6), we identify the upper layer of the moraine as the seismic bedrock. We take the larger and deeper part of the valley as the resonating valley. For this part, we read a depth of around 82 m and a half-width of 290 m from the figure. For the borehole profile in the Kurpark (Fig. 7), the seismic bedrock depth corresponds to 62 m. Using the values of the seismic profile, we obtain

$$f = 1.74\frac{v_S}{4h}, \tag{2}$$

i.e. the 2-dimensional resonance frequency would be 74 % larger than the 1-dimensional resonance frequency, and in any case always larger than the latter.
We observed 1.11 Hz for the 2-dimensional valley resonance in the KUR array and 1.25 Hz in the KON array, but an ellipticity peak frequency of around 1.5 Hz for all stations. If we identify the polarization frequency as the fundamental frequency of the 2-dimensional valley resonance and the ellipticity peak as the 1-dimensional resonance, this does not fit well.
Using the the measured resonance frequency of 1.11 Hz in the Kurpark, the average shear-wave velocity of the sedimentary layers can be calculated as 209 m/s with the depth of the seismic profile. Using the depth of the borehole profile, the resulting average shear-wave velocity would be 158 m/s.

5.4 3-component high-resolution FK

The results of the 3-component high-resolution FK analysis (Poggi and Fäh, 2010) of the KON and KUR arrays are shown in Figs 17 and 18. On the vertical component, the fundamental mode of the Rayleigh waves is clearly visible for both the KON and the KUR array. For the KON array, a higher mode is also visible. On the radial components of the KON array, the fundamental mode is not so easy to identify, but a higher mode can be seen. For the KUR array, part of the fundamental mode and part of a harmonic mode are distinguishable. On the transverse components of the KON array, the fundamental mode is clearly visible below 6 Hz. At higher frequencies, it is unclear if the succession of the fundamental or of a harmonic mode are seen. For the KUR array, the fundamental transverse mode is clearly identified, and a harmonic mode of unclear order can also be seen.

The ellipticity curves determined with the 3-component HRFK analysis are shown in Fig. 18.
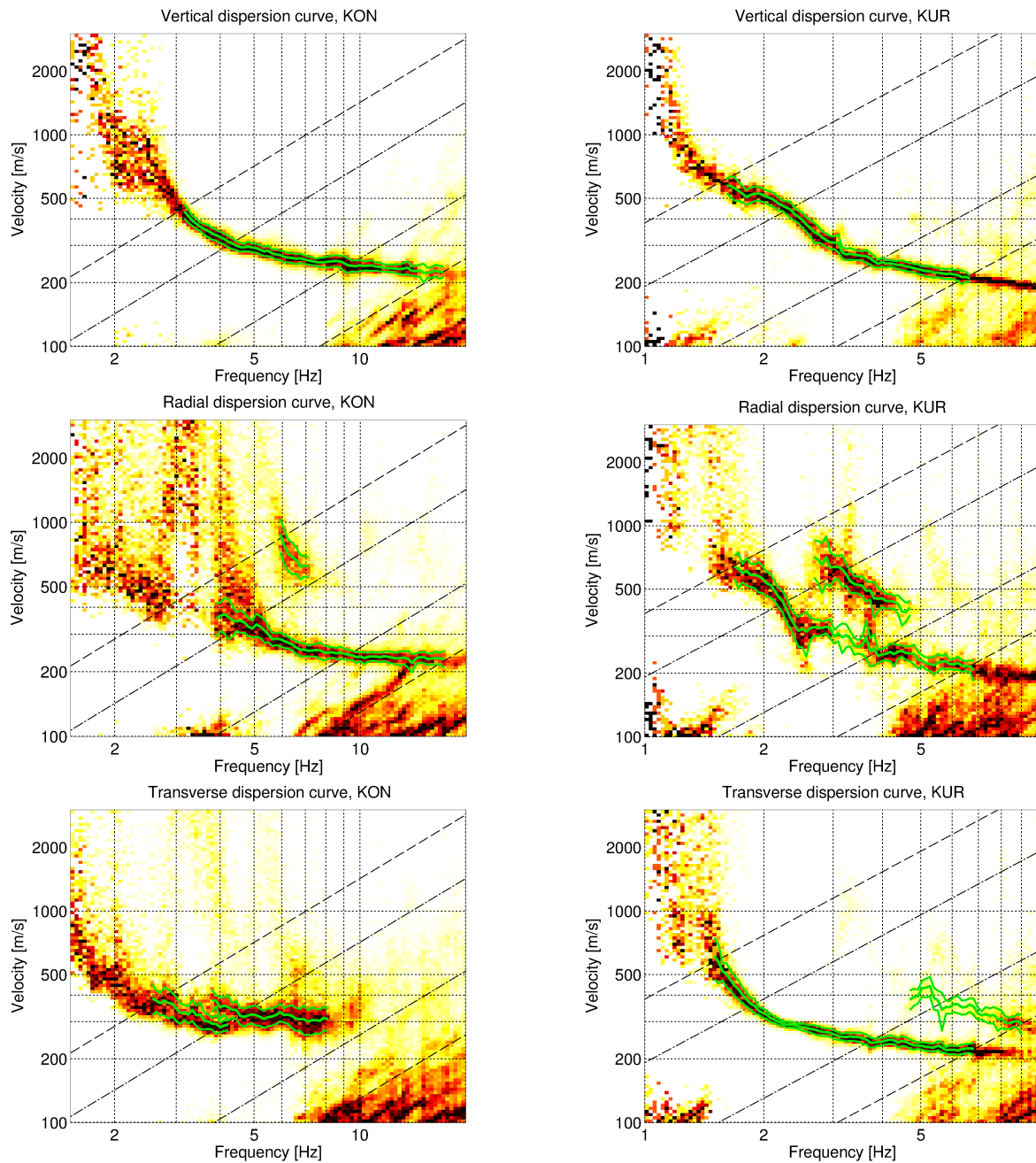
Figure 17: Dispersion curves obtained with the 3-component HRFK algorithm (Poggi and Fäh, 2010). In the left column, the results for the first array (KON) are shown, in the right column for the second array (KUR). The lines from top to bottom show the results for the vertical, radial and transverse components, respectively. The dashed and dotted black lines are the array resolution limits. The solid green lines are picked from the data, where the central line indicates the best values and the two outer lines the standard deviation.
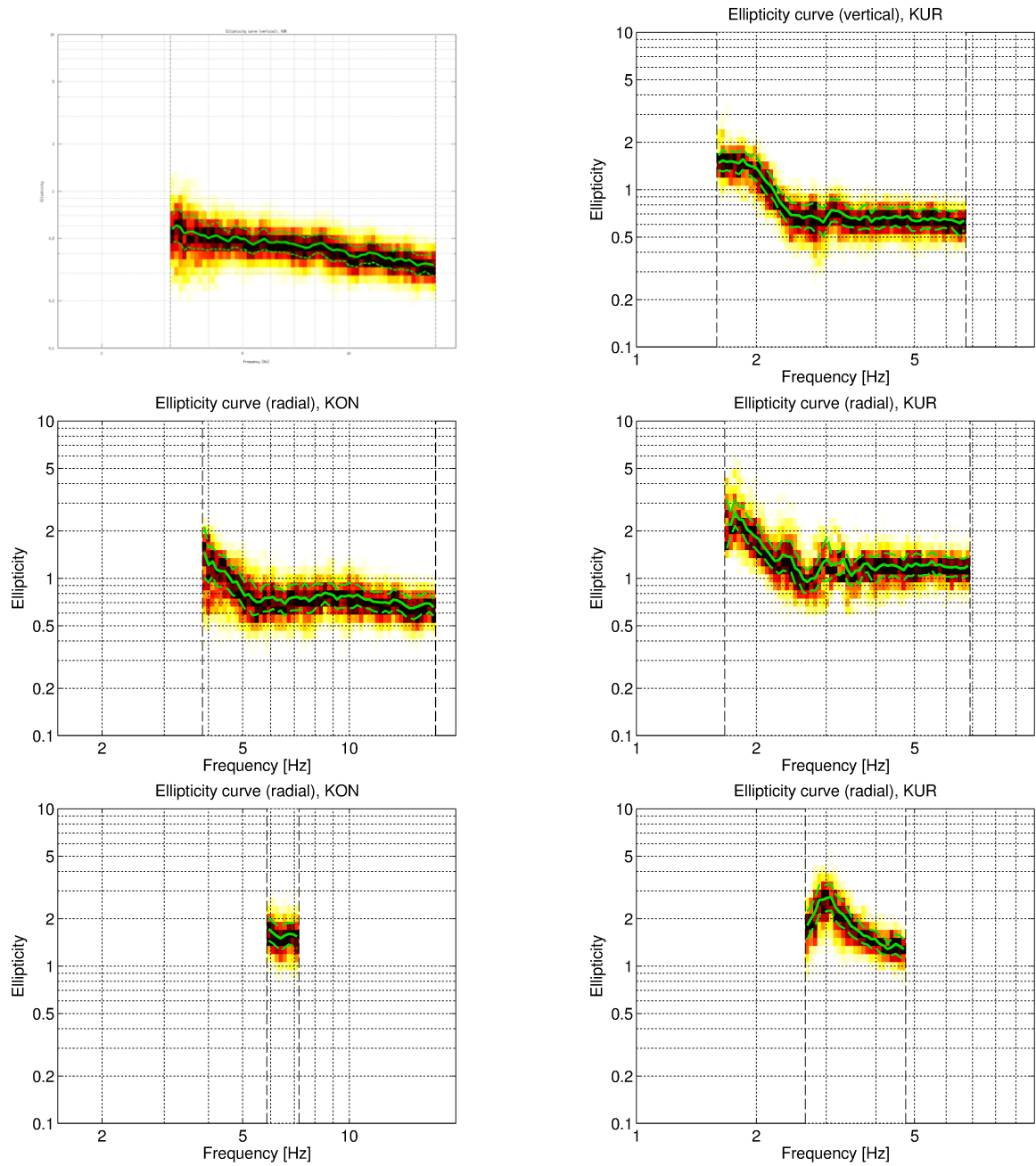
Figure 18: Ellipticity curves obtained with the 3-component HRFK algorithm (Poggi and Fäh, 2010) for the KON array (left) and the KUR array (right). The frequency ranges of the different curves correspond to the ranges where the dispersion curves had been picked. Top: Results for the vertical component. Center: Results for the first mode of the radial component. Bottom: Results for the second mode of the radial component.

5.5 WaveDec

The results of the WaveDec (Maranò et al., 2012) processing are shown in Figs 19 - 22. This technique estimates the properties of single or multiple waves simultaneously with a maximum likelihood approach. We applied it once estimating only the properties of a single Love wave (modeling L), once estimating the properties of a single Rayleigh wave (modeling R) and once estimating one Love and one Rayleigh wave in the same time (modeling LR), both for the KON and the KUR arrays.

As can be seen in Fig. 19, the Love waves are not well retrieved in the KON array. However, it is still possible to pick dispersion curves inside the resolution limits of the array. In the KUR array, however, the Love wave dispersion curve of the fundamental mode can be retrieved in the whole array resolution limits. Higher modes are not detected. The results of the L and LR modelings are very similar.

Rayleigh wave dispersion curves are well retrieved in the KON and the KUR arrays (see Fig. 20), both times inside the complete range of the array resolution limits. There are no major differences between the R and the LR modeling.

The ellipticity curves in Figs 21 and 22 are plotted in two ways. On the left side, the ellipticity angle is shown. On the right side, the ellipticity is shown. The WaveDec code actually estimates the ellipticity angle. Ellipticity is the tangent of this angle. A negative ellipticity angle stands for retrograde particle motion, a positive ellipticity angle for prograde particle motion. In the figure, the ellipticity of only one mode is visible, which we interpret as the fundamental mode. It can be seen that the particle motion is prograde below 3 Hz and retrograde above. This corresponds to the ellipticity trough. The particle motion below the ellipticity peak, which should be retrograde, is not identified. In the ellipticity curves on the right side, automatically picked ellipticity curves are also shown which will be used for comparison reasons with the other techniques later.
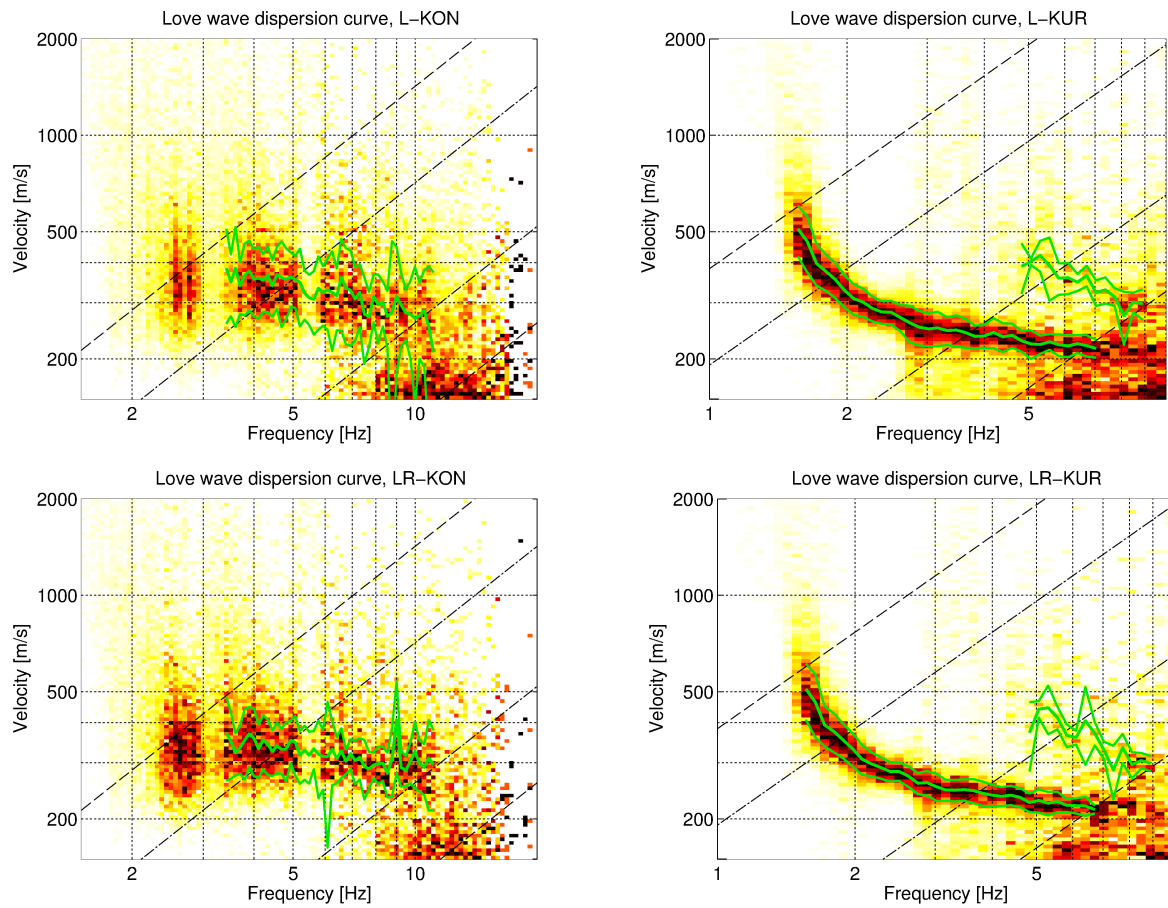
Figure 19: Love wave dispersion curves obtained with the WaveDec technique (Maranò et al., 2012). The first line shows the results for the analysis of only Love waves, the second line for estimating the Love and Rayleigh wave contributions simultaneously. The left plots correspond to the KON array, the right ones to the KUR array. The dashed lines indicate the theoretical array resolution limits.

Figure 20: Rayleigh wave dispersion curves obtained with the WaveDec technique (Maranò et al., 2012). The first line shows the results for the analysis of only Rayleigh waves, the second line for estimating the Love and Rayleigh wave contributions simultaneously. The left plots correspond to the KON array, the right ones to the KUR array. The dashed lines indicate the theoretical array resolution limits.
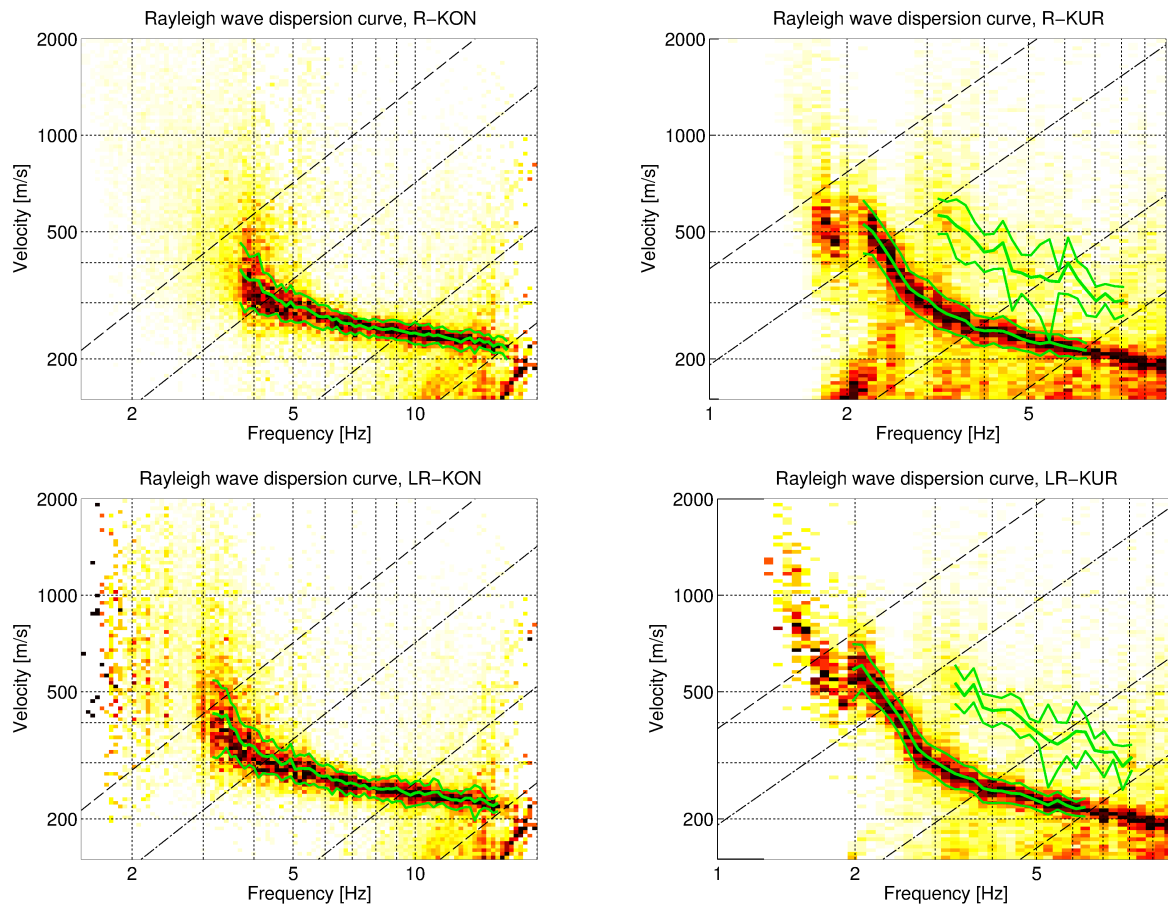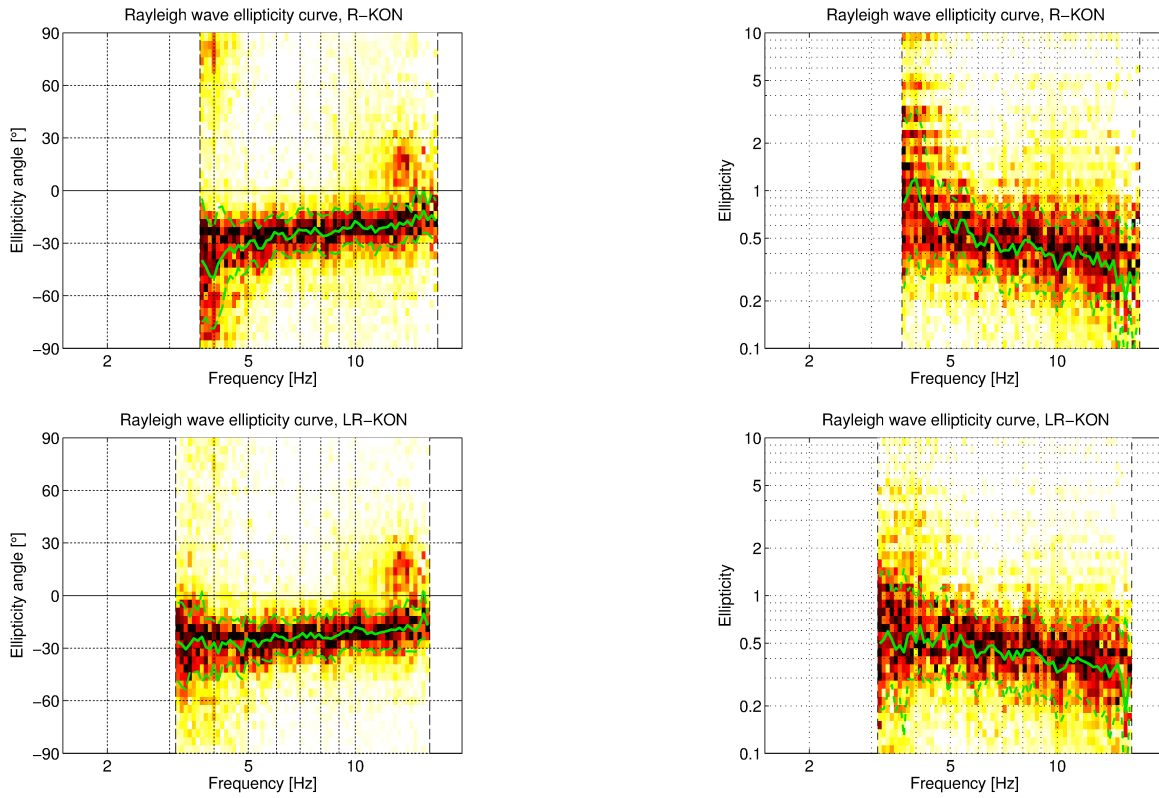
Figure 21: Rayleigh wave ellipticity curves obtained with the WaveDec technique (Maranò et al., 2012) for the KON array. The left column shows the ellipticity angles, the right column the tangent of this angle, i.e. the ellipticity. The different rows show the R and LR analyses.
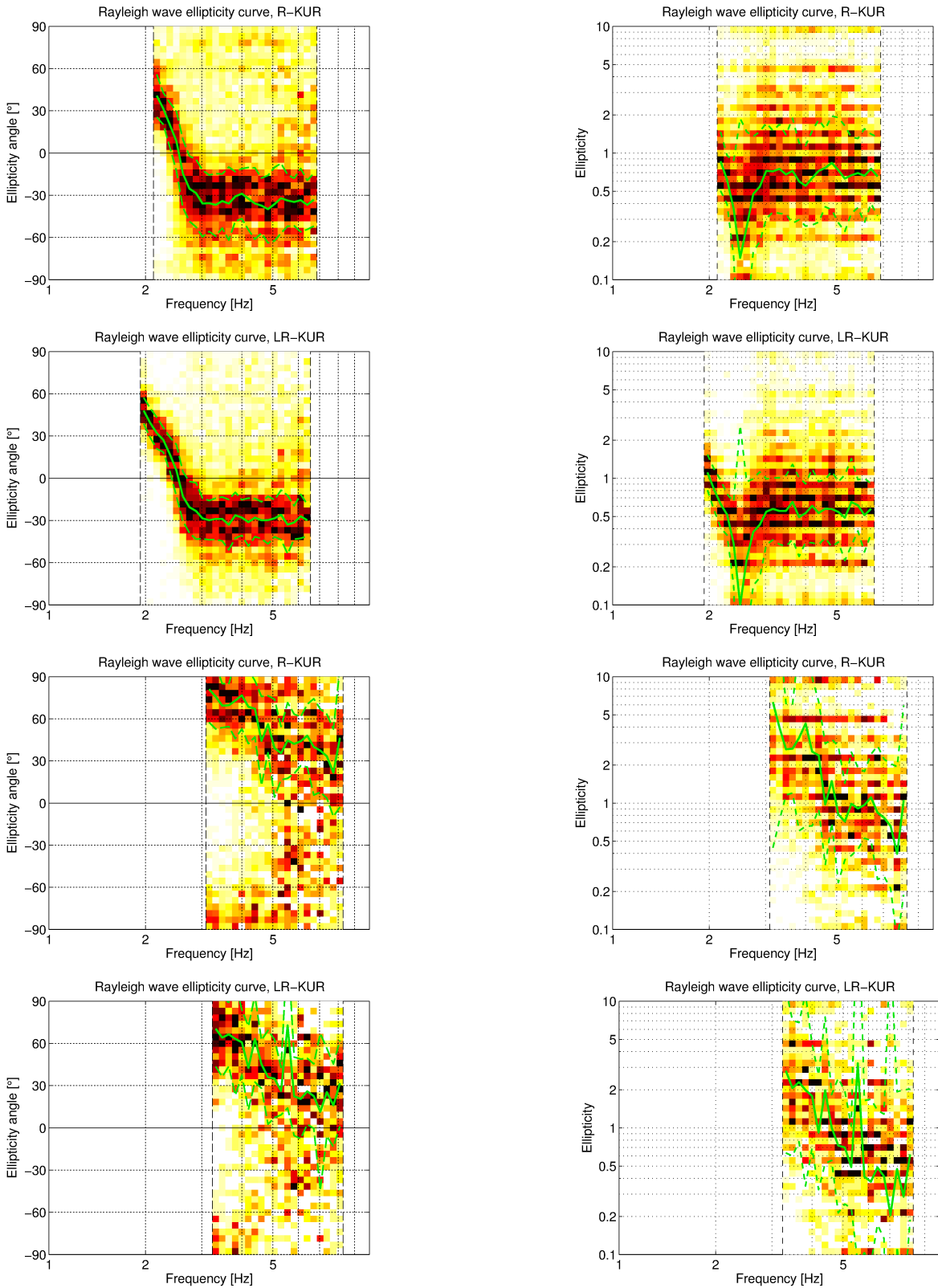
Figure 22: Rayleigh wave ellipticity curves obtained with the WaveDec technique (Maranò et al., 2012) for the KUR array. The left column shows the ellipticity angles, the right column the tangent of this angle, i.e. the ellipticity. The first and second rows show the results for the fundamental mode, the third and fourth rows for the first harmonic mode of the R and LR analyses, respectively.

31

5.6 SPAC

For the KON and KUR measurements, we also calculated the SPAC (Aki, 1957) curves of the vertical components. Actually, we used the M-SPAC (Bettig et al., 2001) technique implemented in geopsy. In order to do so, we defined rings with different radius ranges. For all station pairs with distance inside this radius range, the cross-correlation is calculated in different frequency ranges. These cross-correlation curves are averaged for all station pairs of the respective ring and give the SPAC curve. The rings are defined in such a way that at least three station pairs contribute and that their connecting vectors have a good directional coverage. The different rings and station pairs are shown in Fig. 23. Finally, for the KON array, six rings with distances between 10 and about 50 m have been defined. In the KUR array, we defined seven rings with distances between 20 and 130 m.

The SPAC curves for all these rings are shown in Figs 24 and 25 for the KON and KUR arrays, respectively. The black points indicate the data values which contributed to the final dispersion curve estimation, which was made with the function `spac2disp` of the geopsy package. These resulting dispersion curves are shown in Fig. 26. For the KON array, the dispersion curve is retrieved between 2.8 and 7.2 Hz. In the KUR array, it is retrieved between 2.0 and 9.5 Hz.
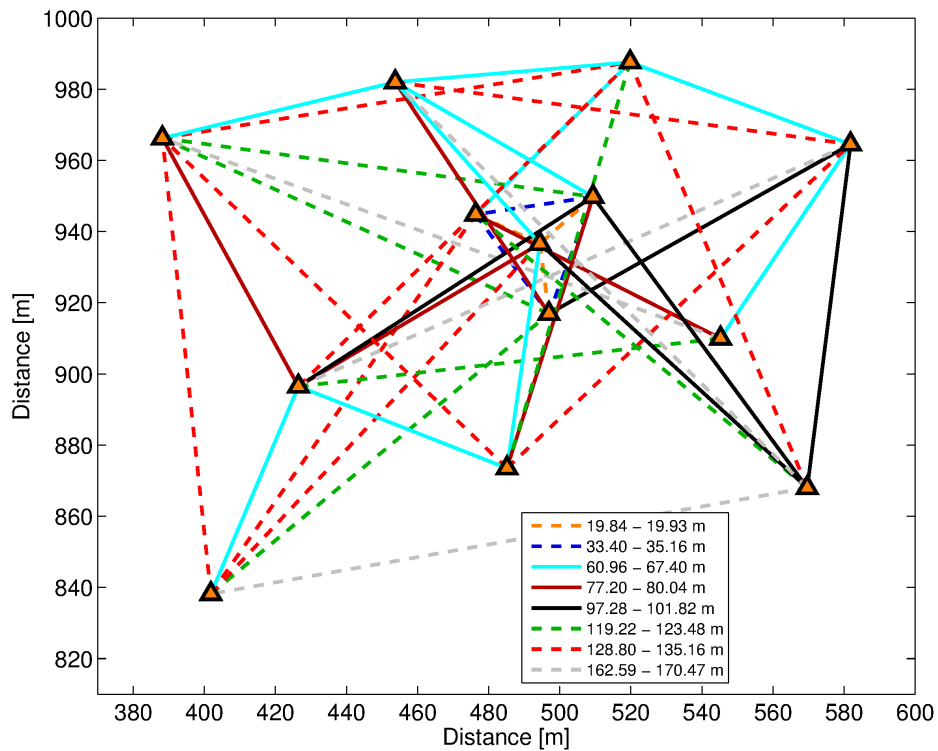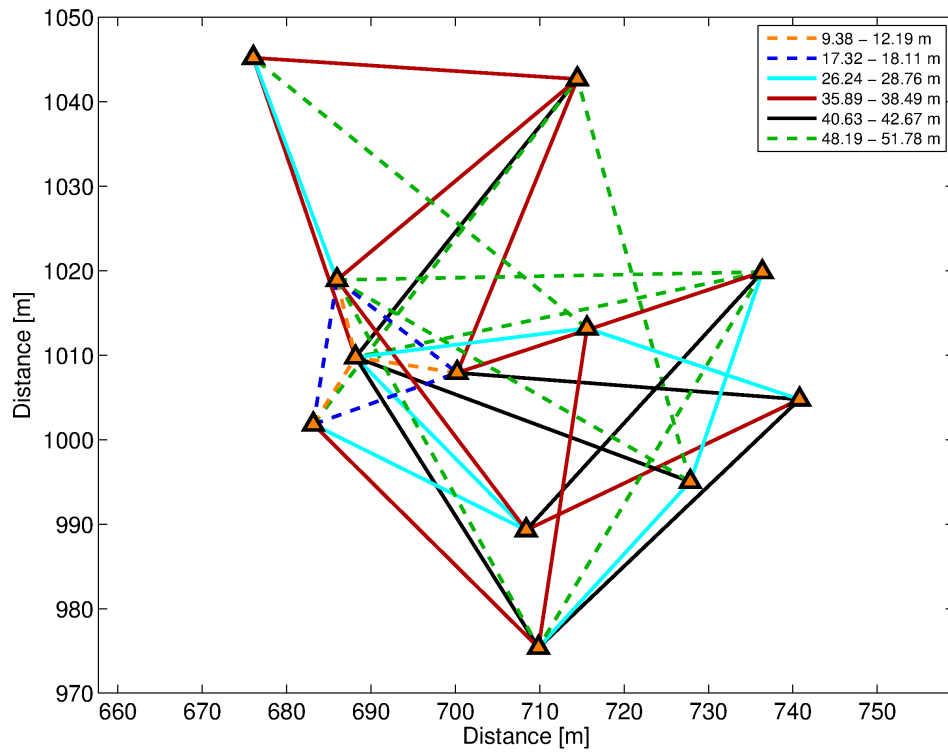
Figure 23: Layout of the KON array (top) and the KUR array (bottom) with the station pairs contributing to the SPAC measurements in the different distance ranges.
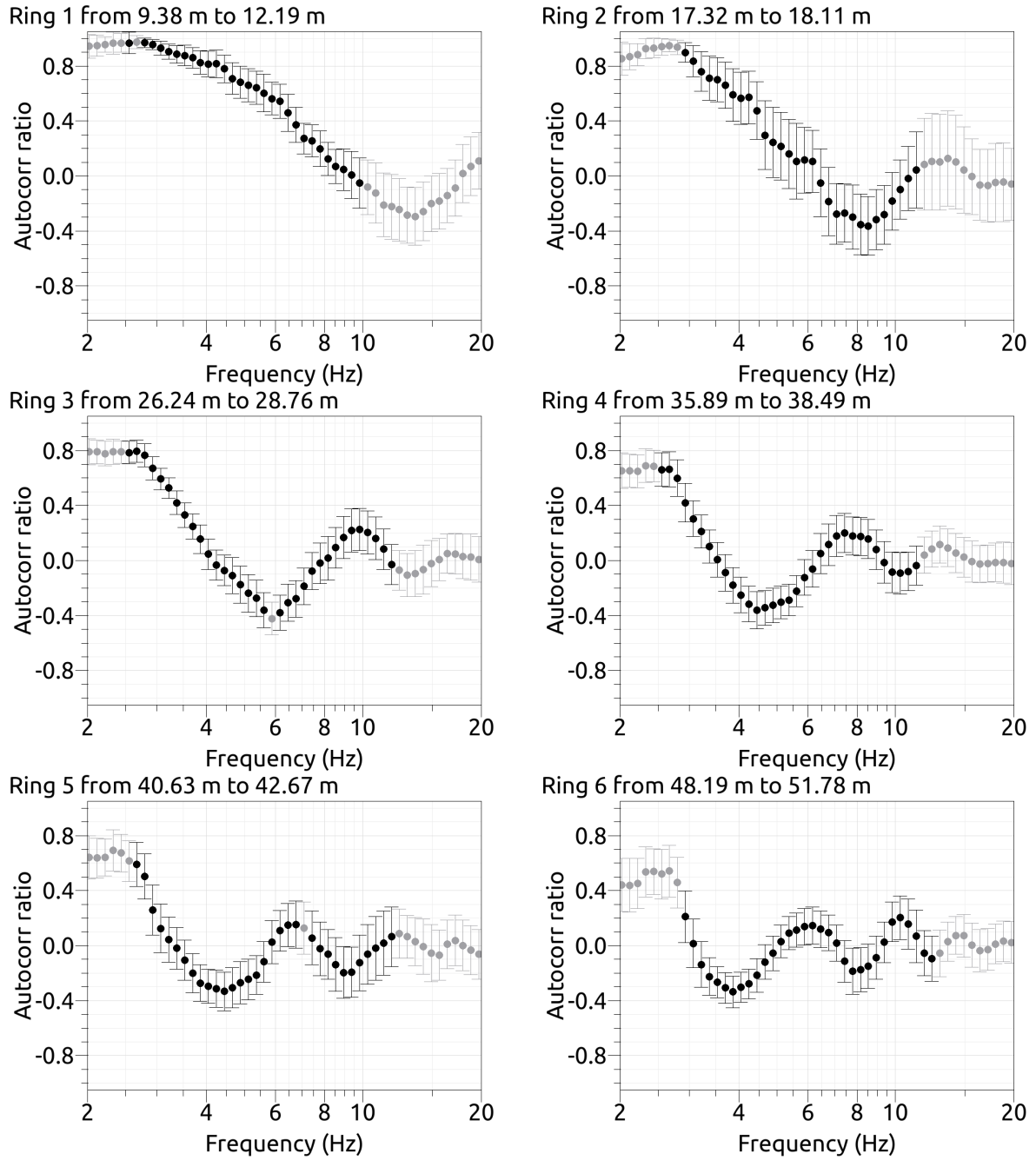
Figure 24: SPAC curves for the KON measurement. The black data points contributed to the dispersion curve estimation.
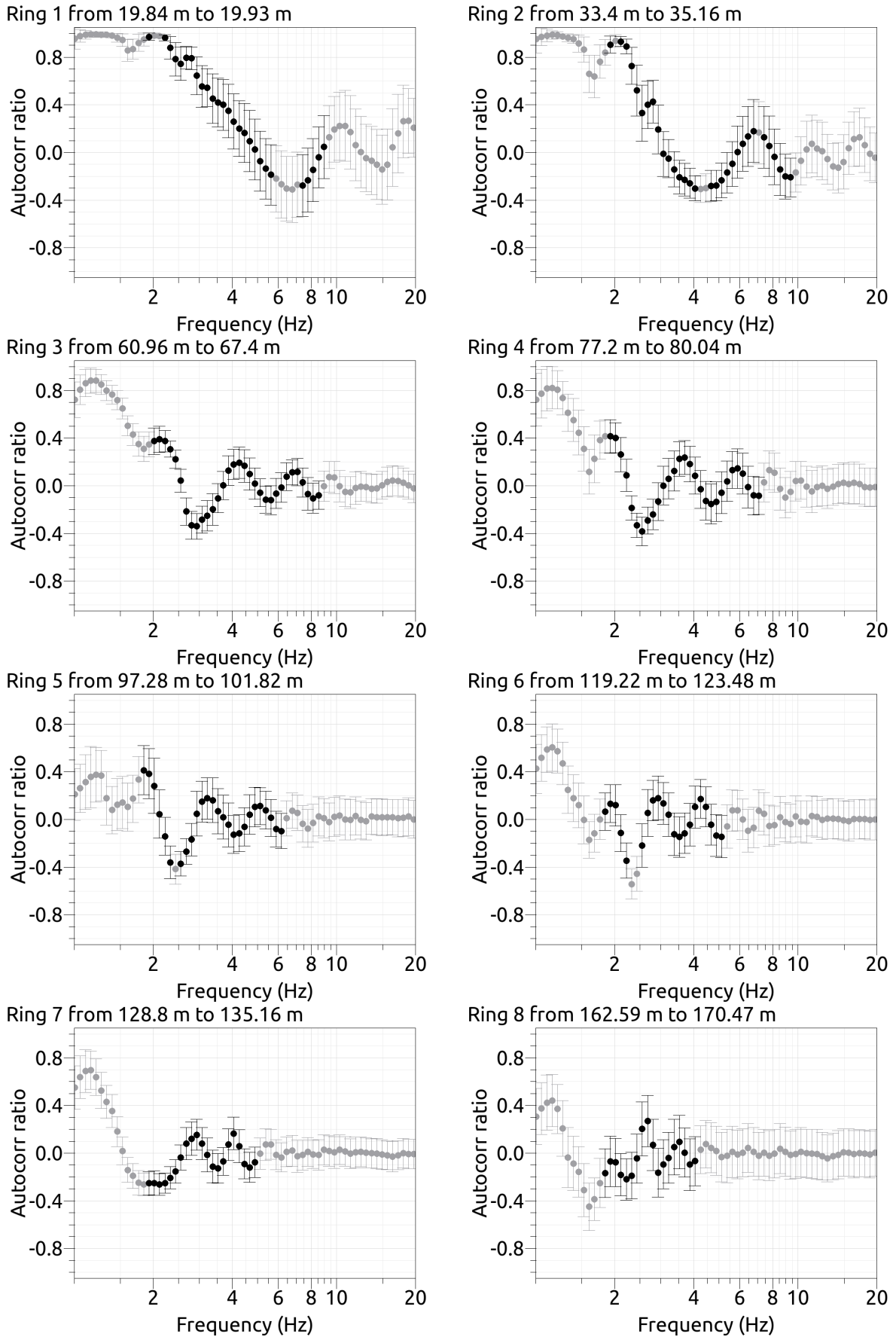
Figure 25: SPAC curves for the KUR measurement. The black data points contributed to the dispersion curve estimation.
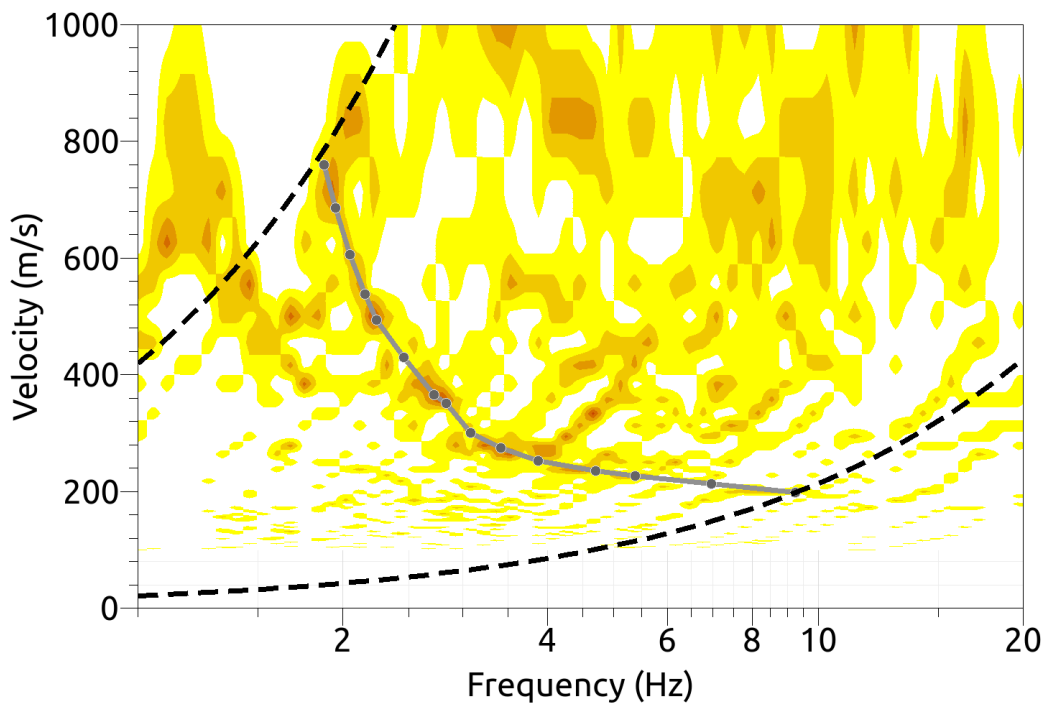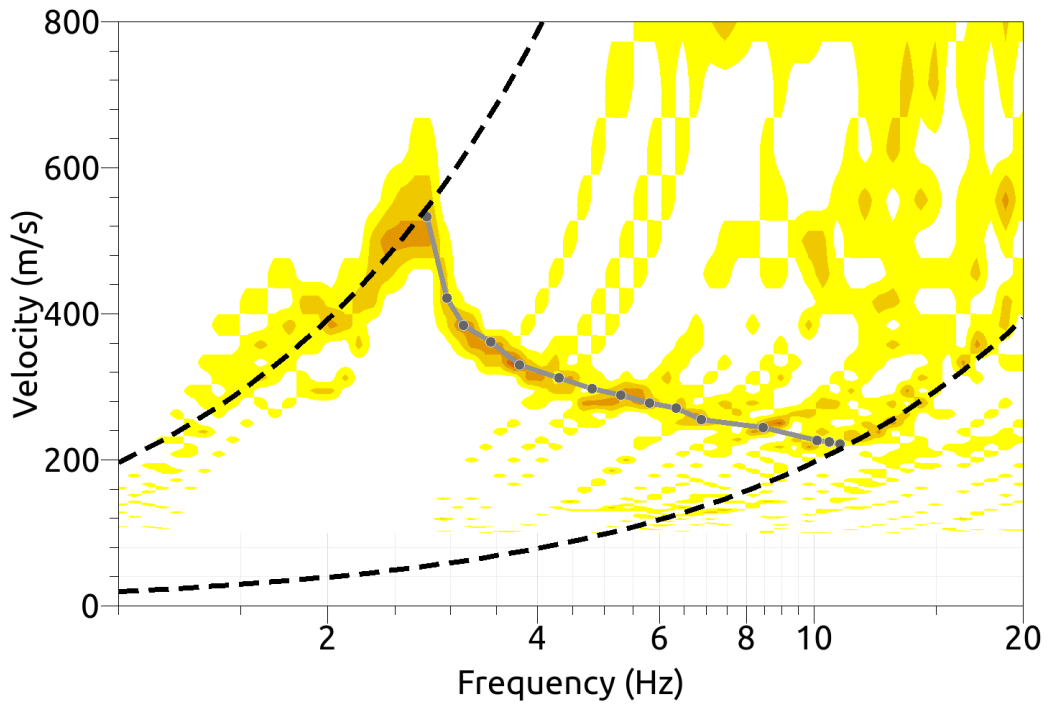
Figure 26: Resulting Rayleigh wave velocities for the KON (top) and the KUR (bottom) measurements. The gray line corresponds to the picked dispersion curve. The black curves are resolution limits, which are different from the FK analysis resolution limits.

5.7 Summary

Fig. 27 gives an overview of the dispersion and ellipticity curves determined by the different methods. The Love wave dispersion curves for the different methods in array KON are compatible for higher frequencies. With the high-resolution FK, there is another mode visible below 4 Hz which cannot be seen with WaveDec. Around 4 Hz, the other curves are clearly distinct from this curve and therefore their mode character is unclear. In the KUR array, HRFK and WaveDec yield virtually the same dispersion curves for both the fundamental and harmonic Love wave modes.

For the fundamental Rayleigh wave mode in the KON array, all methods are in very good agreement. HRFK yields a higher mode here, but its nature is unclear and it is not visible by other methods. In the KUR array, the Rayleigh wave dispersion curves of the fundamental mode are in good agreement for all methods above 3 Hz, but differ a lot at lower frequencies. The WaveDec results are in better agreement with the SPAC measurements and seem more reasonable than the HRFK results here. HRFK and WaveDec both find a higher Rayleigh wave mode.

The ellipticity curves of the different methods differ more than the dispersion curves. In the KON array, the fundamental frequency is too low for the array resolution and therefore the HRFK and WaveDec curves cannot be well compared with the RayDec curve resulting from a single-station measurement. Furthermore, the RayDec result corresponds to station 3, which is the closest to station SDAK, but not the most representative for the array.

In the KUR array, the HRFK ellipticity at least partly coincides with the RayDec ellipticity curve. The WaveDec results are in very good agreement with the RayDec curve and indicate the ellipticity trough nicely. However, even in this large array, the peak frequency is unfortunately outside the range of the array resolution.
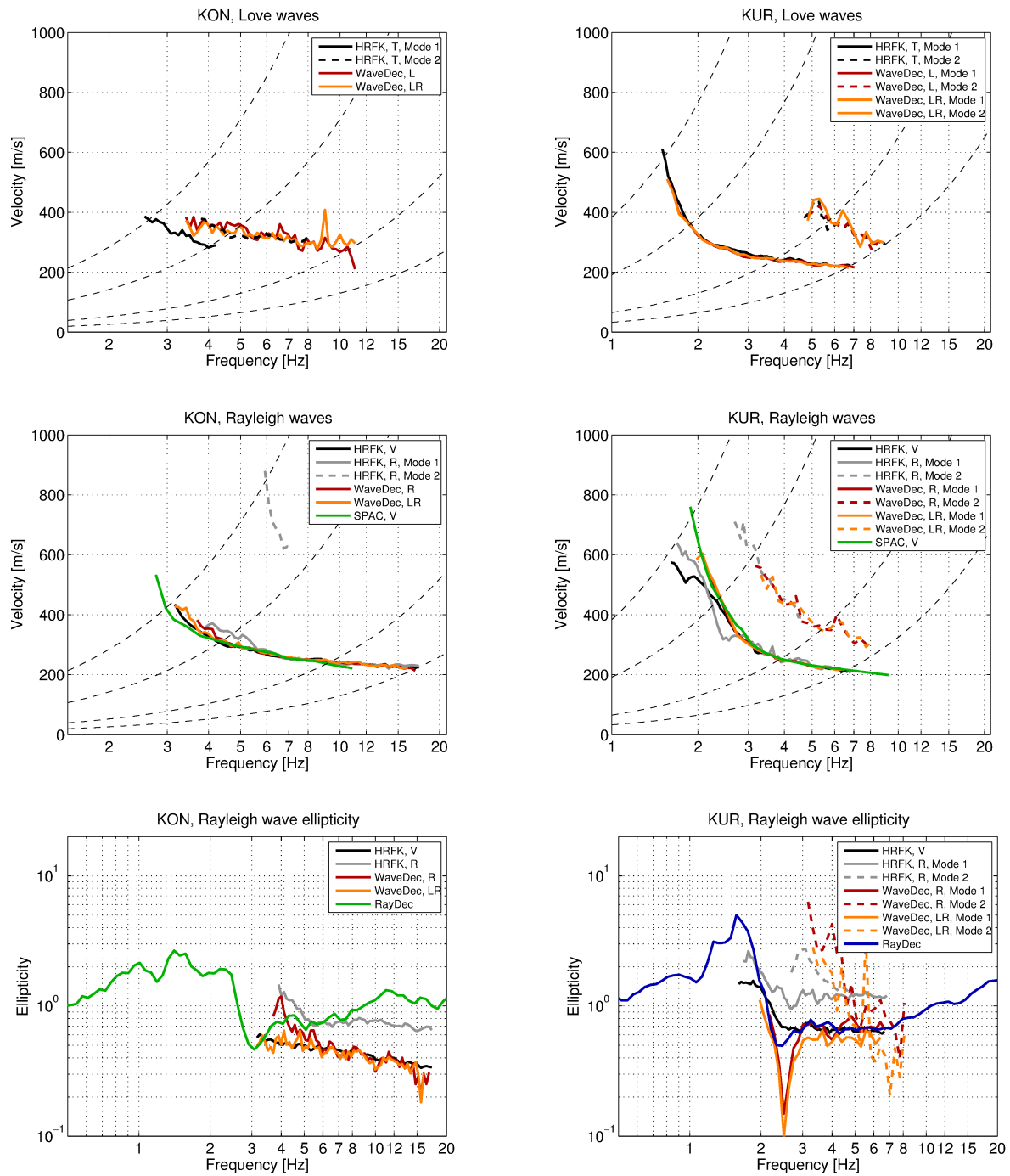
Figure 27: Overview of the Love and Rayleigh wave dispersion curves as well as the ellipticity curves for the KON and the KUR arrays. The dashed lines indicate the theoretical resolution limits of the respective arrays. The RayDec ellipticity curves correspond to station 2 of the KON array and station 12 of the KUR array, respectively.

6 Data inversion

6.1 Inversion data

Before the local soil structure can be retrieved, single dispersion and ellipticity curves need to be defined. Unfortunately, the dispersion curves of the KON and the KUR array differ in such a way that they cannot be combined to a single dispersion curve. Therefore, we perform the inversions for both arrays separately and interpret the results afterwards. As inversion targets, we used the dispersion curves of the fundamental modes of Love and Rayleigh waves for both arrays and the first harmonic modes of Love and Rayleigh waves for the KUR array only, together with the ellipticity curve of the fundamental Rayleigh wave mode. For the KON array, we used the following curves for the dispersion curves:

- HRFK transverse fundamental mode as fundamental Love wave dispersion curve

- HRFK vertical fundamental mode as fundamental Rayleigh wave dispersion curve

For the KUR array, we used these dispersion curves:

- HRFK transverse fundamental mode as fundamental Love wave dispersion curve

- WaveDec LR fundamental mode as fundamental Rayleigh wave dispersion curve

- HRFK transverse harmonic mode as first harmonic Love wave dispersion curve

- HRFK radial harmonic mode as first harmonic Rayleigh wave dispersion curve (not for all inversions)

For the ellipticity curves, the RayDec curves of station 3 in the KON array and station 12 of the KUR array are taken as the best measurement. The right flank of the curves is used for the inversion, as well as a part of the curve above the trough for the KUR case. The peak frequency in the inversions corresponds well with the ones of the H/V measurements and therefore, there is no need to include a part of the left flank of the peak. As the first harmonic Rayleigh wave dispersion curve is not well fitted in the KUR inversion, we also performed another inversion without this curve.

The data curves that have been used for the inversion are indicated in Table 2 and are shown in Fig. 28.
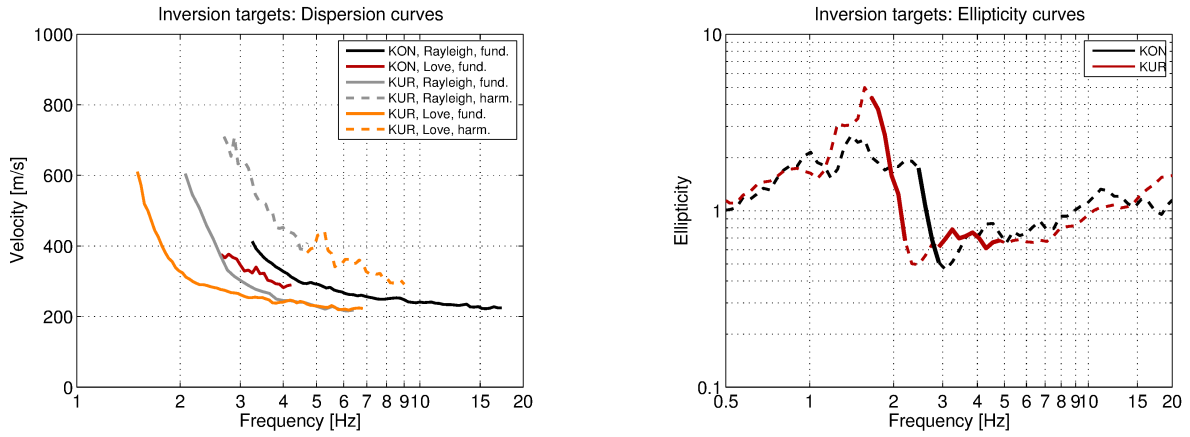
Figure 28: Overview of the dispersion and ellipticity curves used as targets for the different inversions.

Table 2: List of the data curves used as targets in the inversions.

Array	Wave type	Mode	Curve type	Frequency range [Hz]
KON	Love	fundamental	dispersion	2.63 - 4.15
KON	Rayleigh	fundamental	dispersion	3.25 - 17.20
KON	Rayleigh	fundamental	ellipticity	2.47 - 2.80
KUR	Love	fundamental	dispersion	1.51 - 6.74
KUR	Love	harmonic	dispersion	4.75 - 8.91
KUR	Rayleigh	fundamental	dispersion	2.00 - 6.29
KUR	Rayleigh	harmonic	dispersion	2.71 - 4.65
KUR	Rayleigh	fundamental	ellipticity	1.66 - 2.21
KUR	Rayleigh	fundamental	ellipticity	2.98 - 4.87

6.1.1 Inversion parameterization

From the geological profile in the Kurpark (see Fig. 7), we expect the underground profile to consist of three layers (including the bedrock). Therefore, such a parameterization is the first inversion parameterization we use. In order to see if more complex models fit our data in a better way, we also performed inversions with more layers. In this way, parameterizations with four, five, six and seven layers have been used. As we did all inversions for the KON and the KUR array separately, this results in a total of ten inversions.

In each parameterization, the first layer's depth could range from 1 to 20 m, the depths of the other layers were allowed to range from 5 to 100 m. The shear-wave velocity of the top layer ranged from 50 to 300 m/s (v_P from 80 to 1 000 m/s), the one of the second layer from 100 to 1 000 m/s (v_P from 100 to 2 000 m/s) and for all other layers from 150 to 3 500 m/s (v_P from 200 to 5 000 m/s). The density was fixed to 2 300 kg/m^3 for the lowest layer and to 2 000 kg/m^3 for all other layers.

6.2 Inversion results

We performed five inversions for each array with different parameterizations (see Table 3). Each inversion run produced 200 000 total models in order to assure a good convergence of the solution. The results of these inversions are shown in Figs. 29 - 38.

The five inversions yielded similar results in both arrays. Because the parameterizations with less parameters are special cases of the seven-layer parameterization, we would expect that the seven-layer inversion fits the data the best and has the lowest misfit value. However, as can be seen in Table 3, there is a general opposite trend to be observed. This indicates that the inversion with more parameters did not fully converge. Anyhow, the misfit values of the different inversions of the respective arrays are very close and we can take all results as valid inversion results which describe the underground structure in a good way.

For the KON array (Figs 29-33), all inversions fit the inversion targets very well. The Rayleigh wave dispersion curve is better fitted than the Love wave dispersion curve. The ellipticity curve is well fitted as well and has a singularity for all parameterizations.

For the KUR inversions (Figs 34-38),the fundamental Rayleigh wave dispersion curve is well fitted, as well as its ellipticity curve. The dispersion curve of the first harmonic mode of the Rayleigh wave is only fitted between 3.5 and 4.5 Hz, but not accurately at lower frequencies. The fundamental Love wave dispersion curve is well retrieved above 2 Hz, but there are major discrepancies at lower frequencies. The dispersion curve of the first harmonic Love wave mode, however, is well retrieved.

Table 3: List of inversions

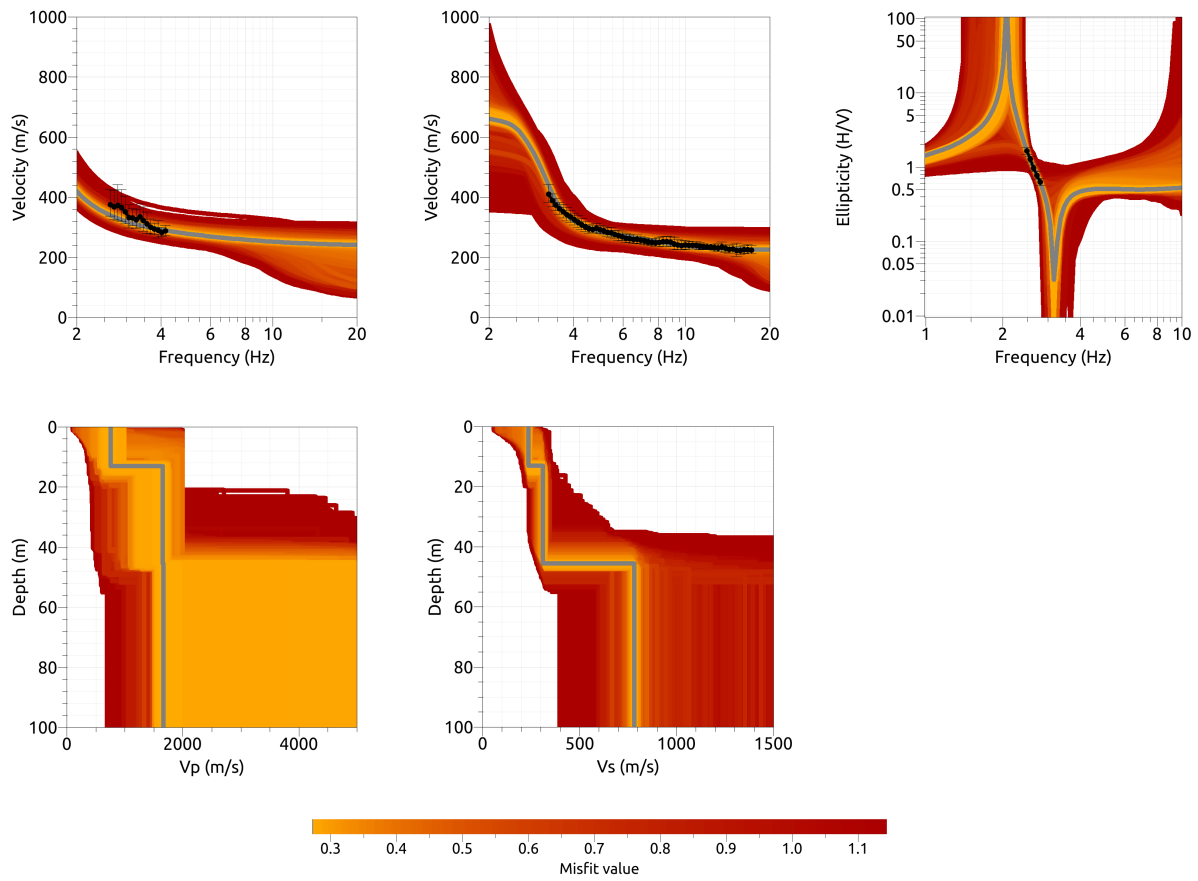| Inversion	Number of layers	Number of models	Minimum misfit
KON03	3	200 000	0.274
KON04	4	200 000	0.286
KON05	5	200 000	0.303
KON06	6	200 000	0.312
KON07	7	200 000	0.301
KUR03	3	200 000	0.696
KUR04	4	200 000	0.696
KUR05	5	200 000	0.713
KUR06	6	200 000	0.720
KUR07	7	200 000	0.737

Figure 29: Inversion KON03: Love wave fundamental mode dispersion curve (top left), Rayleigh wave fundamental mode dispersion curve (top center), Rayleigh wave ellipticity curve (top right), P-wave velocity profiles (center left) and S-wave velocity profiles (center right). The black dots indicate the data points used for the inversion, the gray line indicates the best-fitting model.
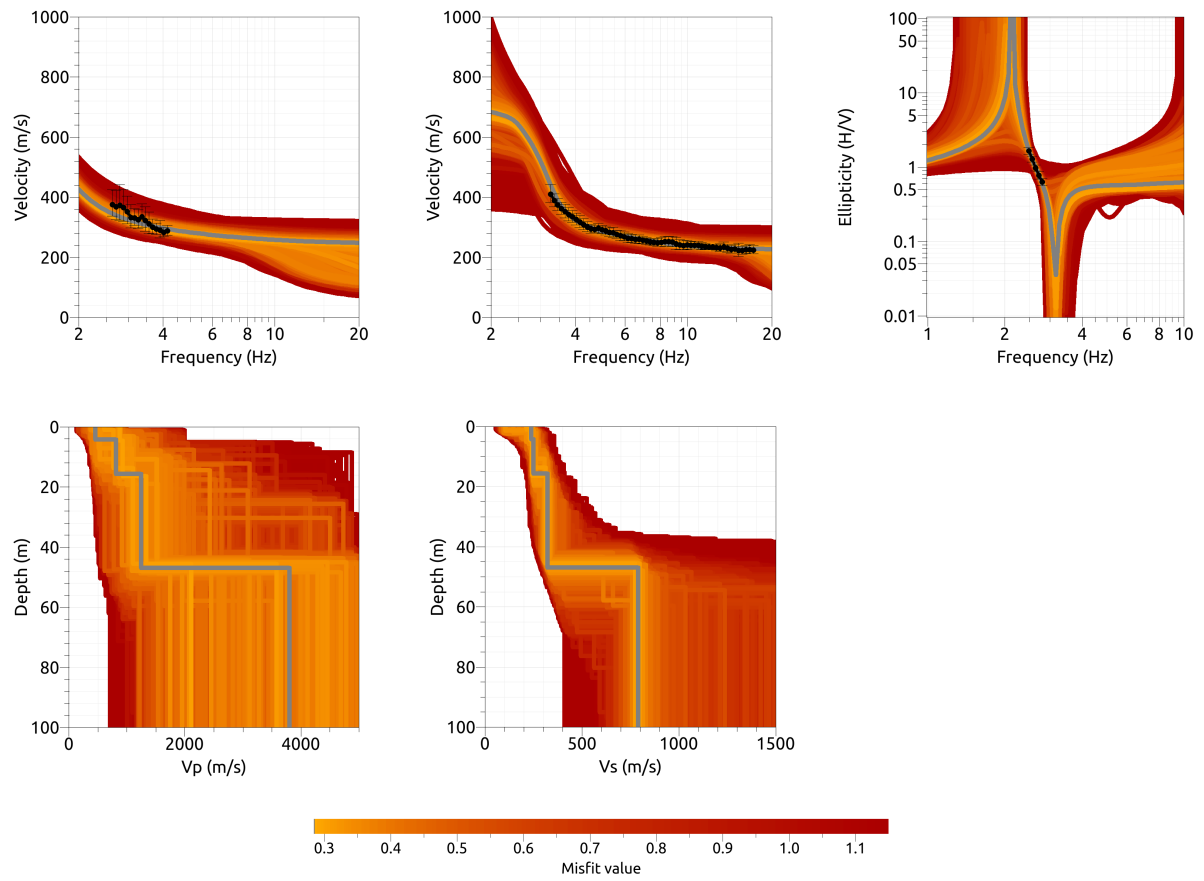
Figure 30: Inversion KON04: Love wave fundamental mode dispersion curve (top left), Rayleigh wave fundamental mode dispersion curve (top center), Rayleigh wave ellipticity curve (top right), P-wave velocity profiles (center left) and S-wave velocity profiles (center right). The black dots indicate the data points used for the inversion, the gray line indicates the best-fitting model.
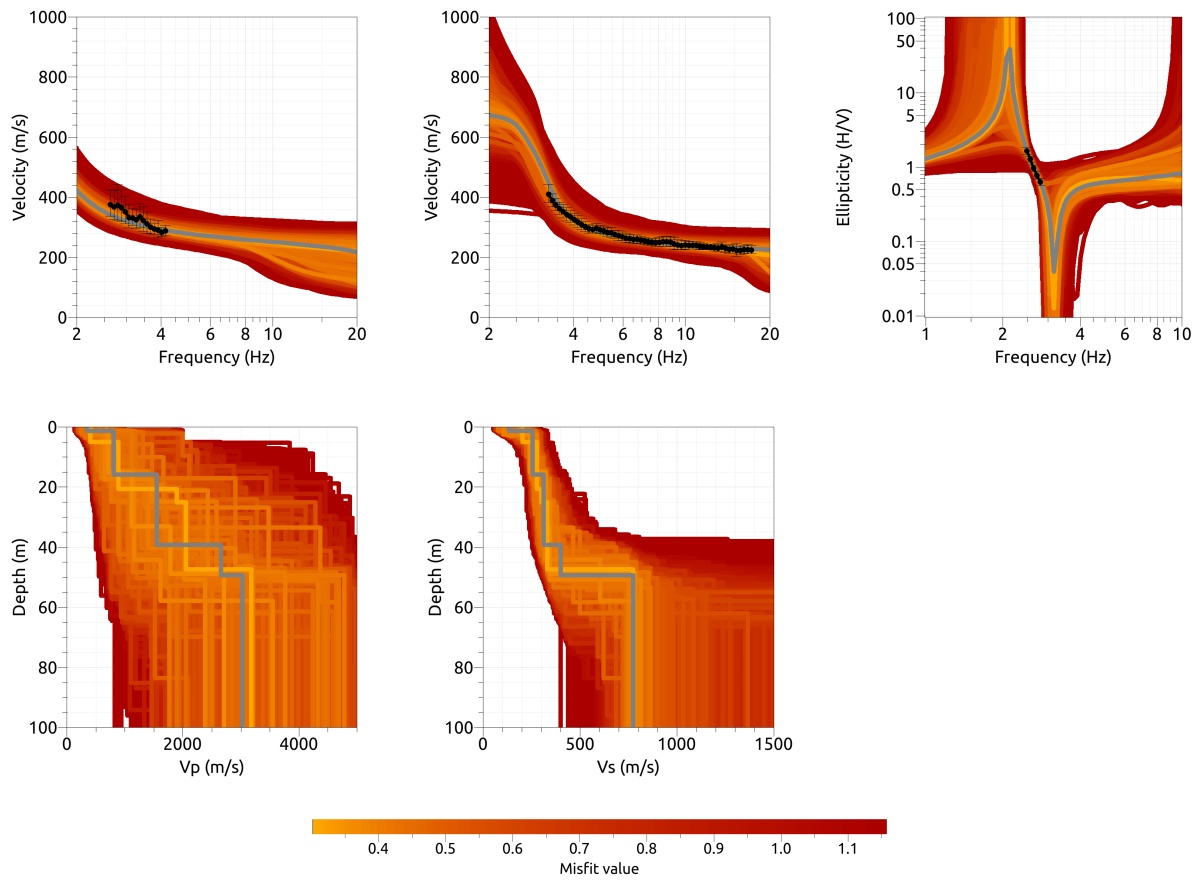
Figure 31: Inversion KON05: Love wave fundamental mode dispersion curve (top left), Rayleigh wave fundamental mode dispersion curve (top center), Rayleigh wave ellipticity curve (top right), P-wave velocity profiles (center left) and S-wave velocity profiles (center right). The black dots indicate the data points used for the inversion, the gray line indicates the best-fitting model.
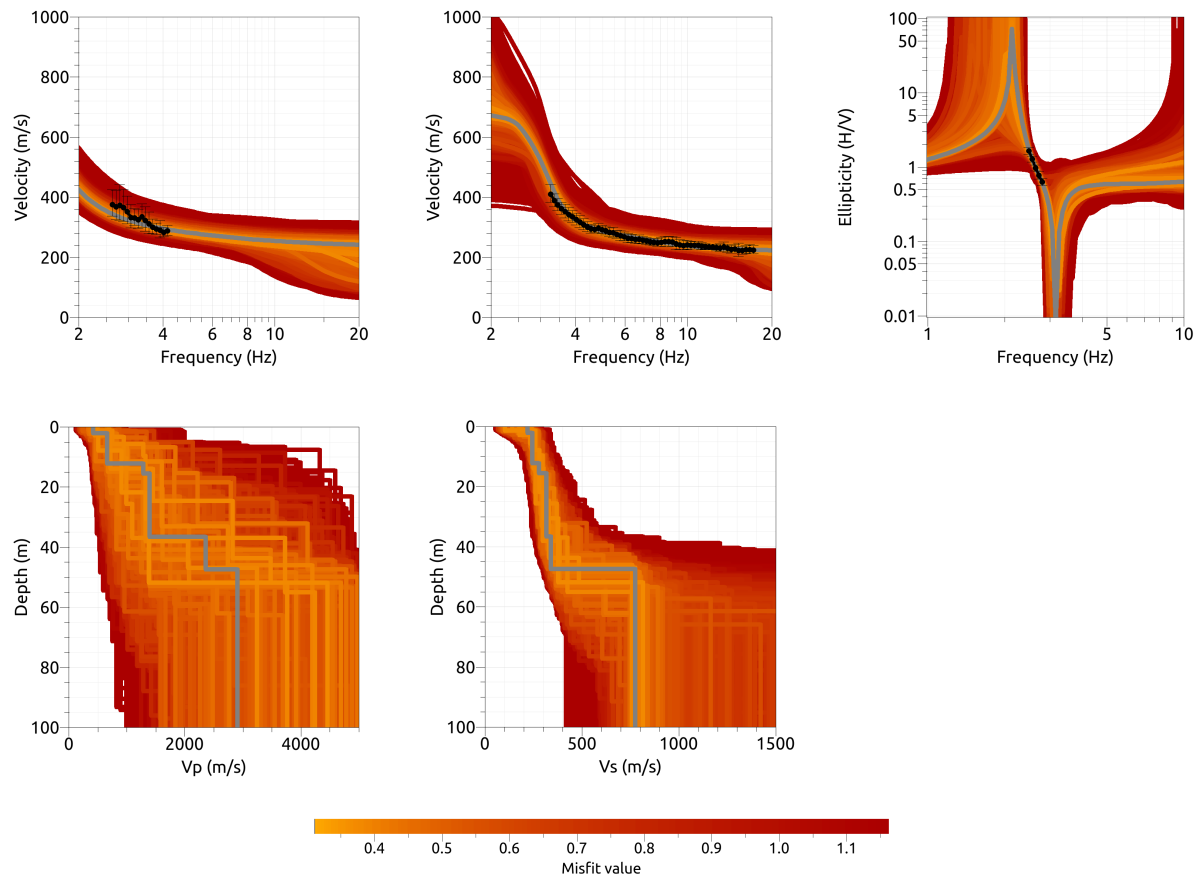
Figure 32: Inversion KON06: Love wave fundamental mode dispersion curve (top left), Rayleigh wave fundamental mode dispersion curve (top center), Rayleigh wave ellipticity curve (top right), P-wave velocity profiles (center left) and S-wave velocity profiles (center right). The black dots indicate the data points used for the inversion, the gray line indicates the best-fitting model.

Figure 33: Inversion KON07: Love wave fundamental mode dispersion curve (top left), Rayleigh wave fundamental mode dispersion curve (top center), Rayleigh wave ellipticity curve (top right), P-wave velocity profiles (center left) and S-wave velocity profiles (center right). The black dots indicate the data points used for the inversion, the gray line indicates the best-fitting model.
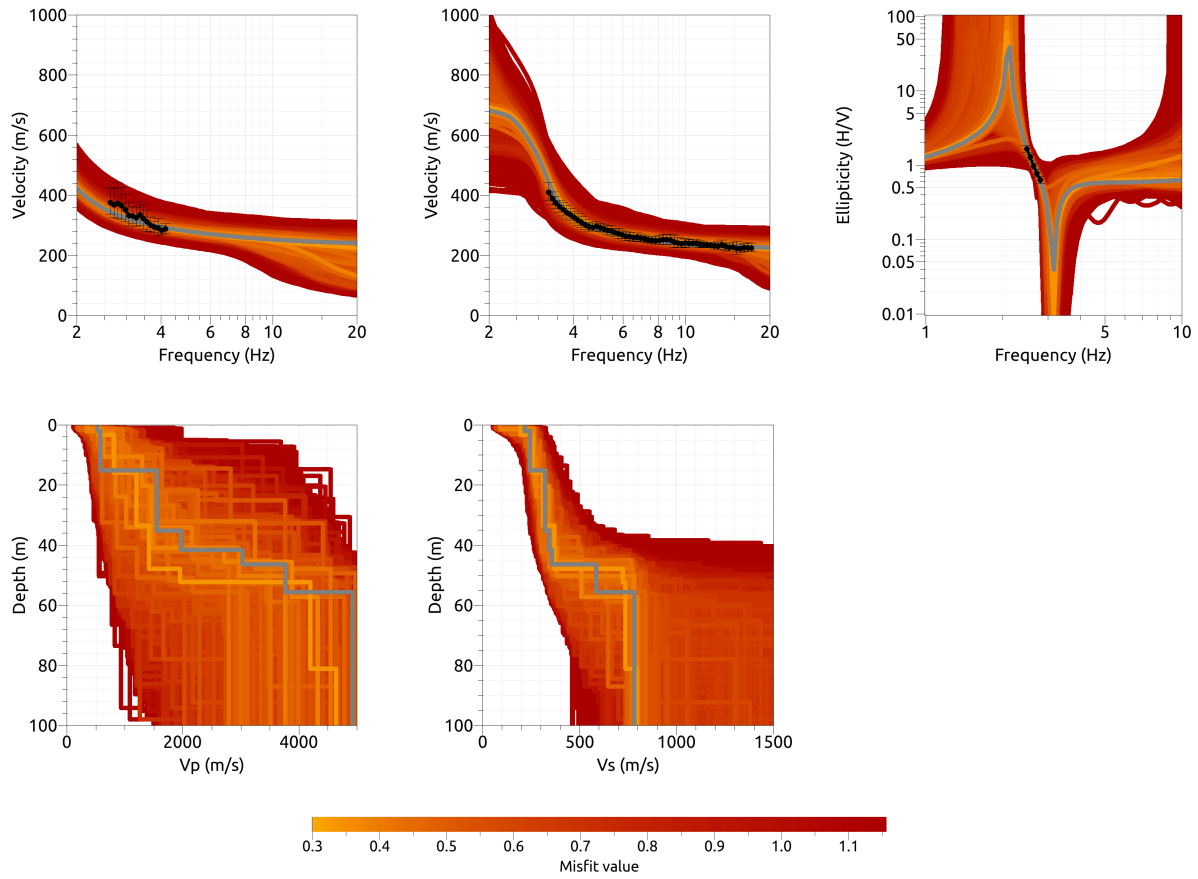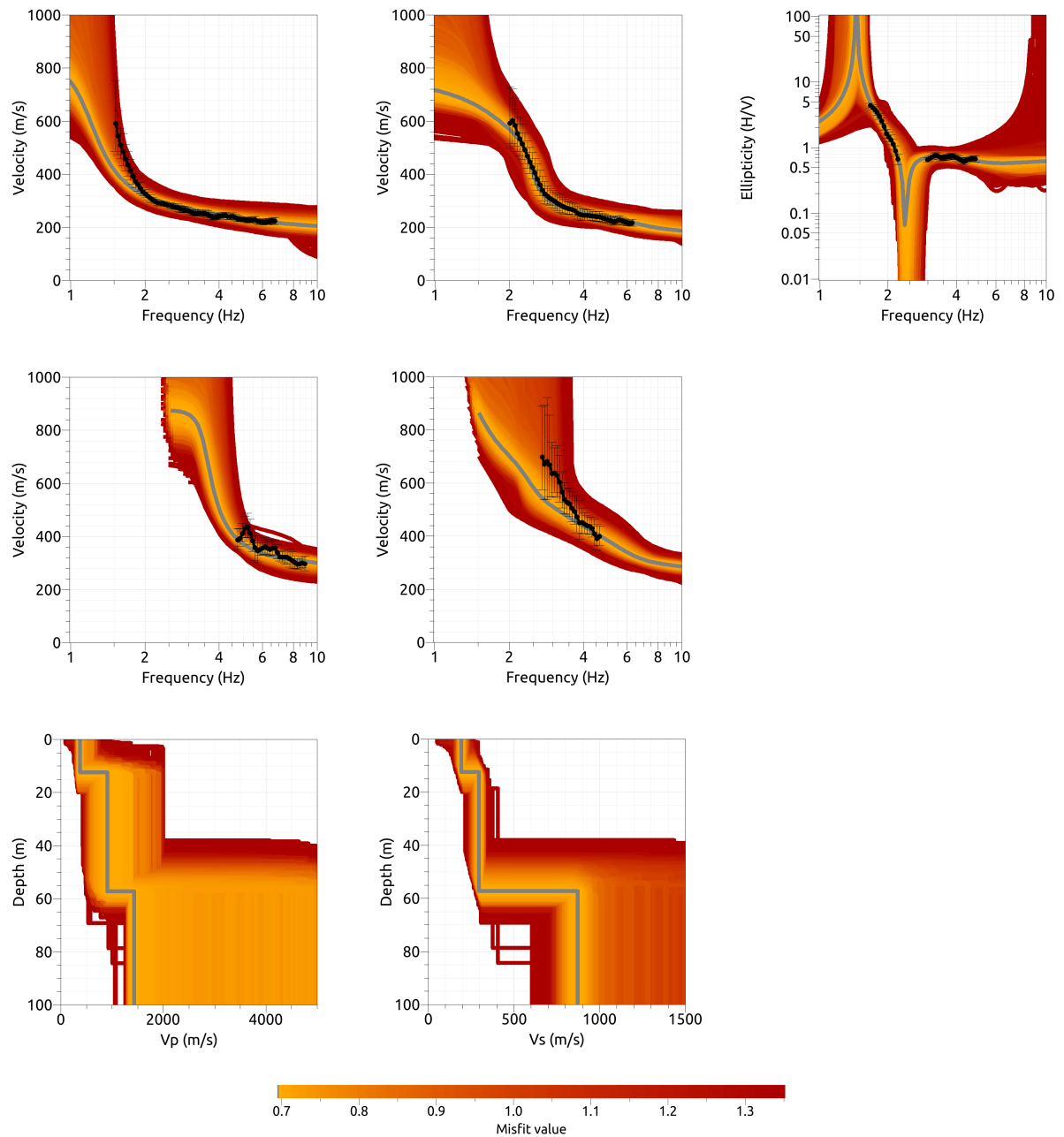
Figure 34: Inversion KUR03: Love wave fundamental mode dispersion curve (top left), Rayleigh wave fundamental mode dispersion curve (top center), Rayleigh wave ellipticity curve (top right), Love wave first higher mode dispersion curve (center left), Rayleigh wave first higher mode dispersion curve (center), P-wave velocity profiles (bottom left) and S-wave velocity profiles (bottom right). The black dots indicate the data points used for the inversion, the gray line indicates the best-fitting model.

47

Figure 35: Inversion KUR04: Love wave fundamental mode dispersion curve (top left), Rayleigh wave fundamental mode dispersion curve (top center), Rayleigh wave ellipticity curve (top right), Love wave first higher mode dispersion curve (center left), P-wave velocity profiles (bottom left) and S-wave velocity profiles (bottom right). The black dots indicate the data points used for the inversion, the gray line indicates the best-fitting model.
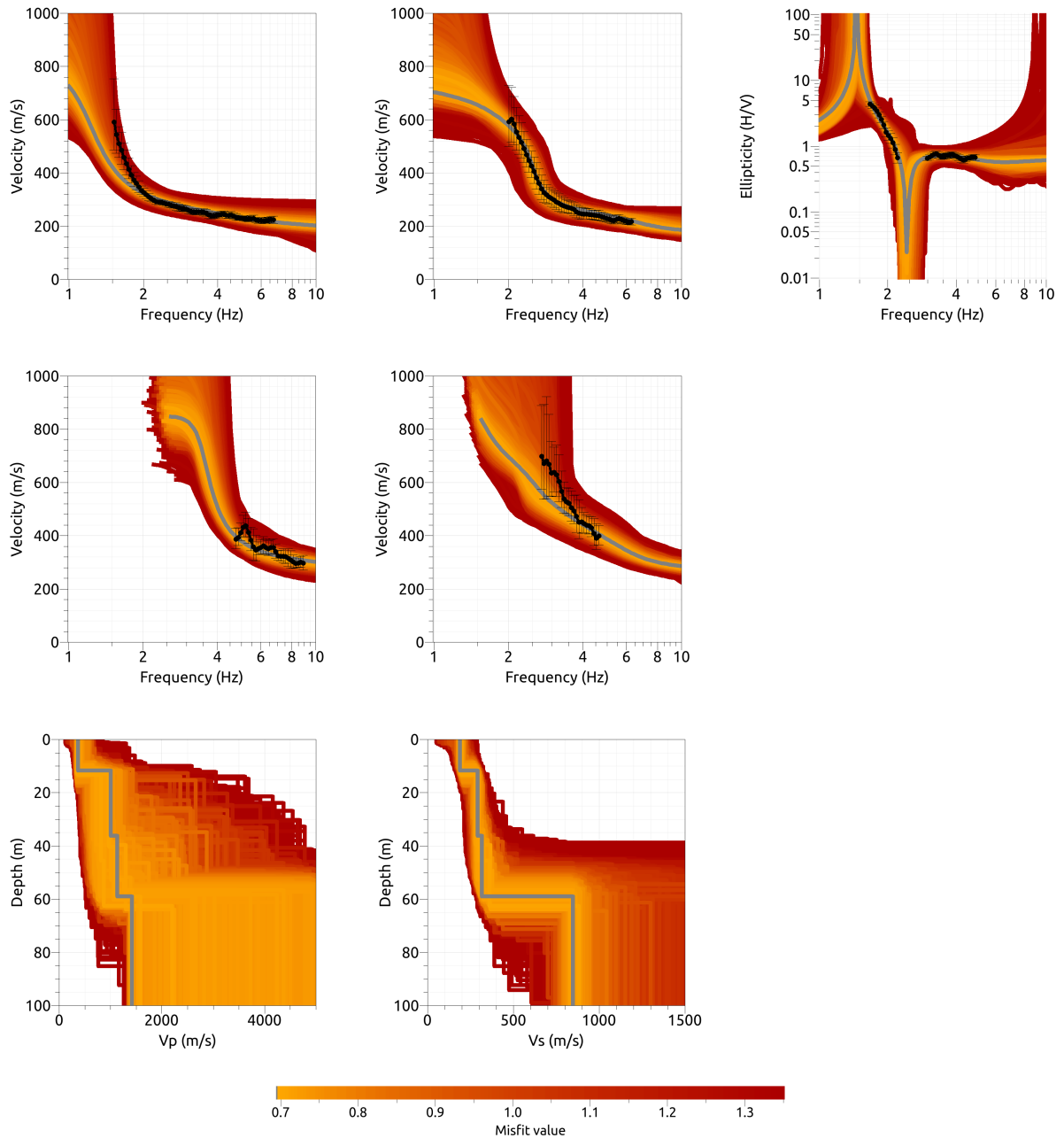
48

Figure 36: Inversion KUR05: Love wave fundamental mode dispersion curve (top left), Rayleigh wave fundamental mode dispersion curve (top center), Rayleigh wave ellipticity curve (top right), Love wave first higher mode dispersion curve (center left), Rayleigh wave first higher mode dispersion curve (center), P-wave velocity profiles (bottom left) and S-wave velocity profiles (bottom right). The black dots indicate the data points used for the inversion, the gray line indicates the best-fitting model.
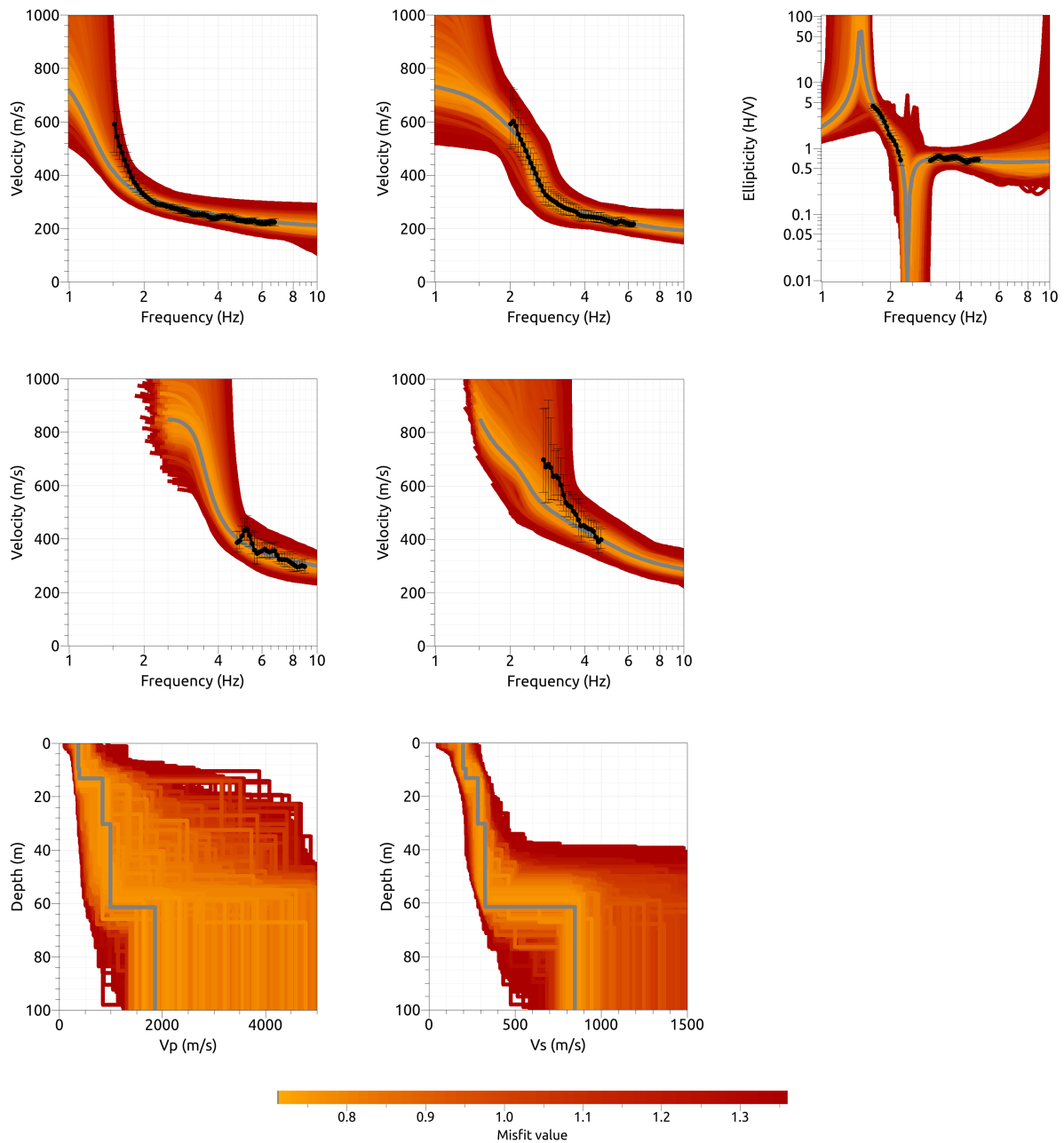
Figure 37: Inversion KUR06: Love wave fundamental mode dispersion curve (top left), Rayleigh wave fundamental mode dispersion curve (top center), Rayleigh wave ellipticity curve (top right), Love wave first higher mode dispersion curve (center left), P-wave velocity profiles (bottom left) and S-wave velocity profiles (bottom right). The black dots indicate the data points used for the inversion, the gray line indicates the best-fitting model.
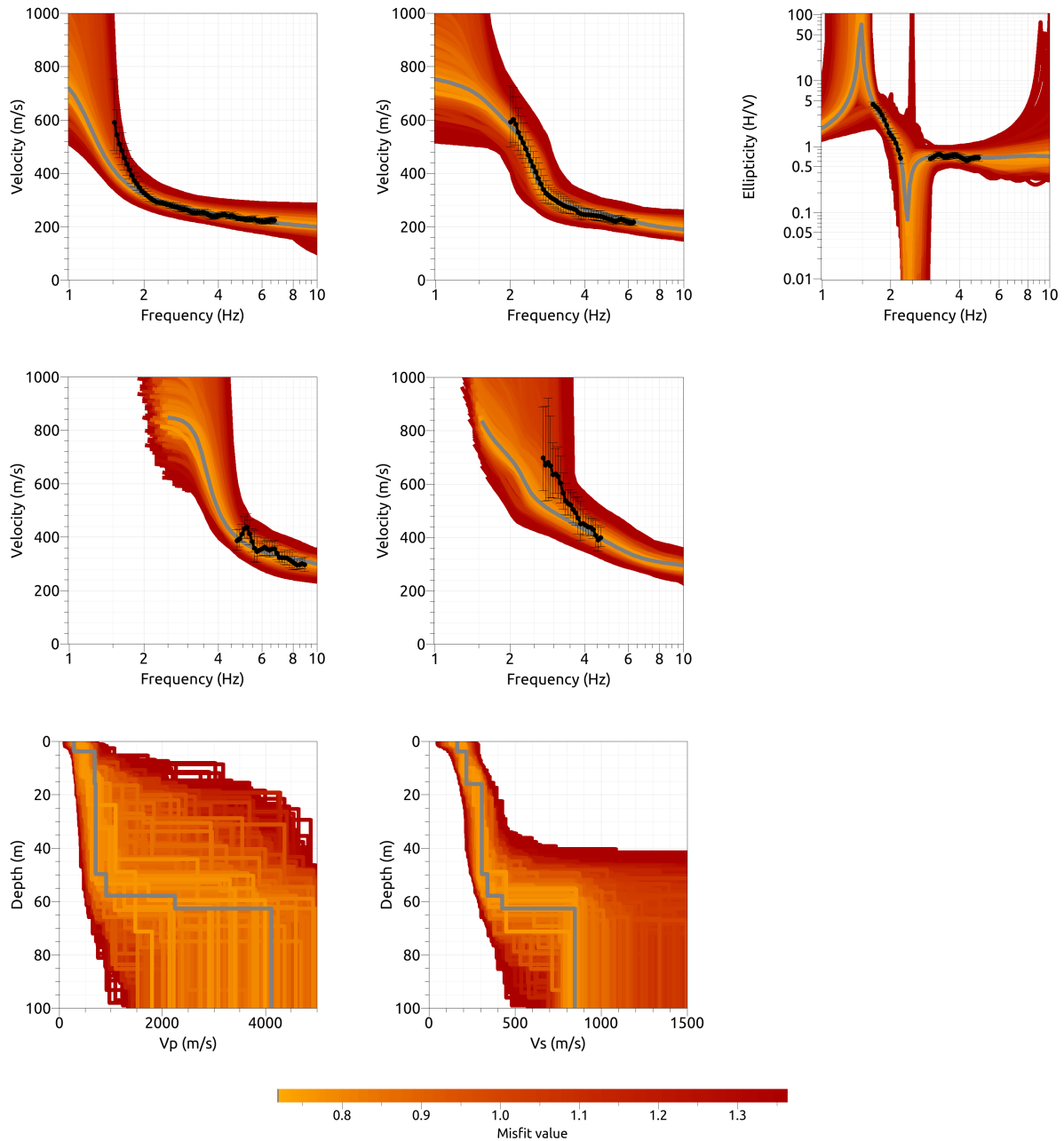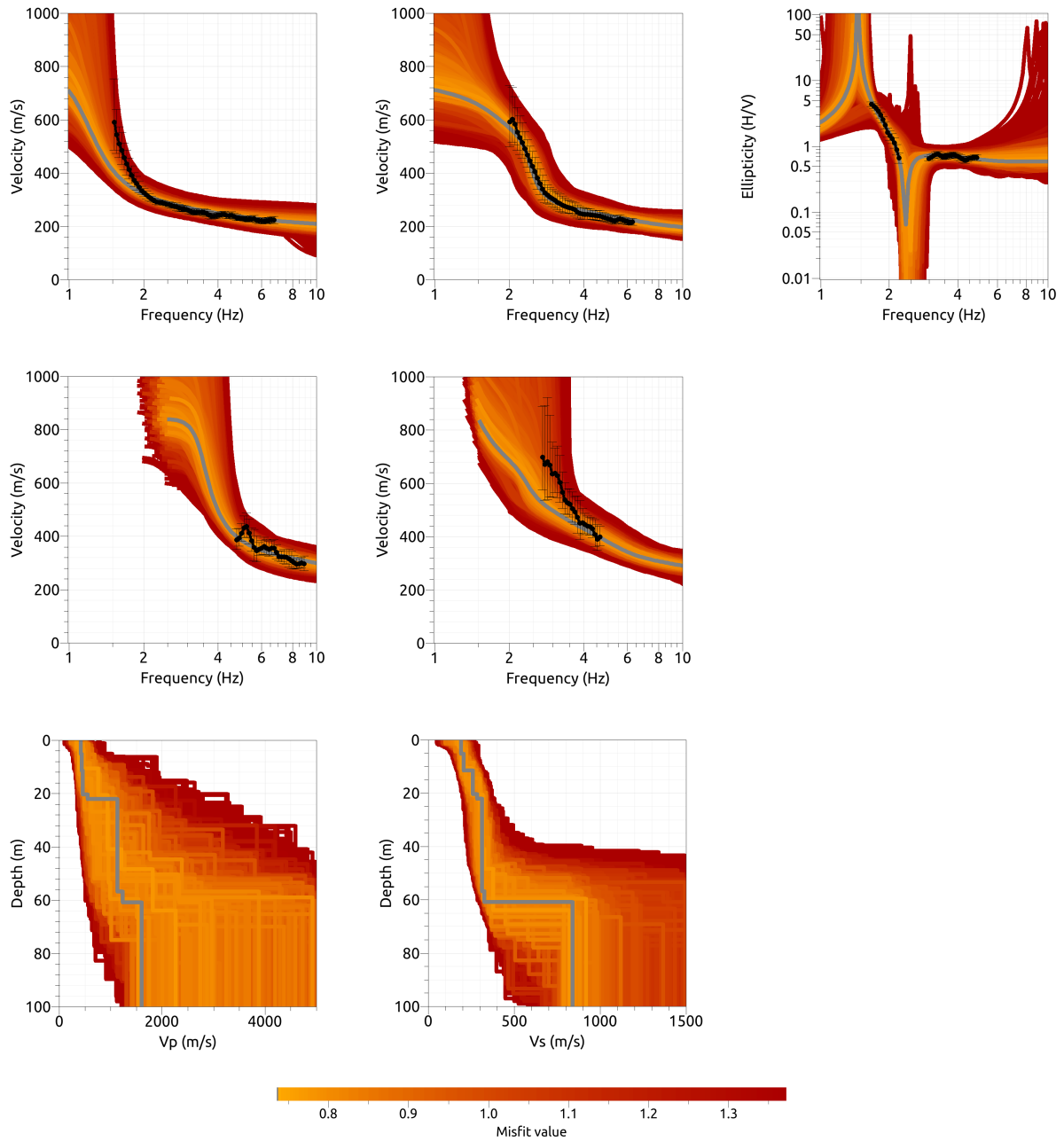
Figure 38: Inversion KUR07: Love wave fundamental mode dispersion curve (top left), Rayleigh wave fundamental mode dispersion curve (top center), Rayleigh wave ellipticity curve (top right), Love wave first higher mode dispersion curve (center left), P-wave velocity profiles (bottom left) and S-wave velocity profiles (bottom right). The black dots indicate the data points used for the inversion, the gray line indicates the best-fitting model.

51

6.2.1 Discussion of the inversion result

The best-fitting models of all inversions are shown in Fig. 39. Even the inversions with more parameters yield results which consist in principle in a three-layer model with slight deviations.

In the KON array, there is a first layer with a shear-wave velovity of around 250 m/s and a thickness of 12 to 16 m, followed by a second layer with a S-wave velocity of around 310 to 320 m/s. The seismic bedrock depth of the different models is between 45 and 49 m, all models yield S-wave velocities in the seismic bedrock of around 790 m/s.

The KUR inversions also yield results which are quite similar. The first layer is around 12 m thick and has a shear-wave velocity of 200 m/s. The second layer has S-wave velocities between 290 and 320 m/s. The seismic bedrock is reached at depths between 57 and 61 m. This is in very good agreement with the borehole profile in the Kurpark.

The profiles below the KON and KUR arrays consist of layers with similar velocities, but different thicknesses. The uppermost layer in the Kurpark is slightly thinner, but the bedrock lies deeper. The depth differences can explain the differences in the ellipticity and dispersion curves in both arrays.

With the knowledge of the borehole profile (Fig. 7), we can give an approximate profile below station SDAK. The first layer consists mainly of gravel ($V_S = 250\,m/s$). The second layer of alluvial deposits (sand and gravel, $V_S = 320\,m/s$) and the seismic bedrock of moraine ($V_S = 790\,m/s$). The underlying geological bedrock of granite cannot be retrieved with our passive measurements.

The average V_{S30} of the best models for the KON array is $274.2 \pm 3.9\,m/s$, in the KUR array it is $242.1 \pm 1.3\,m/s$.
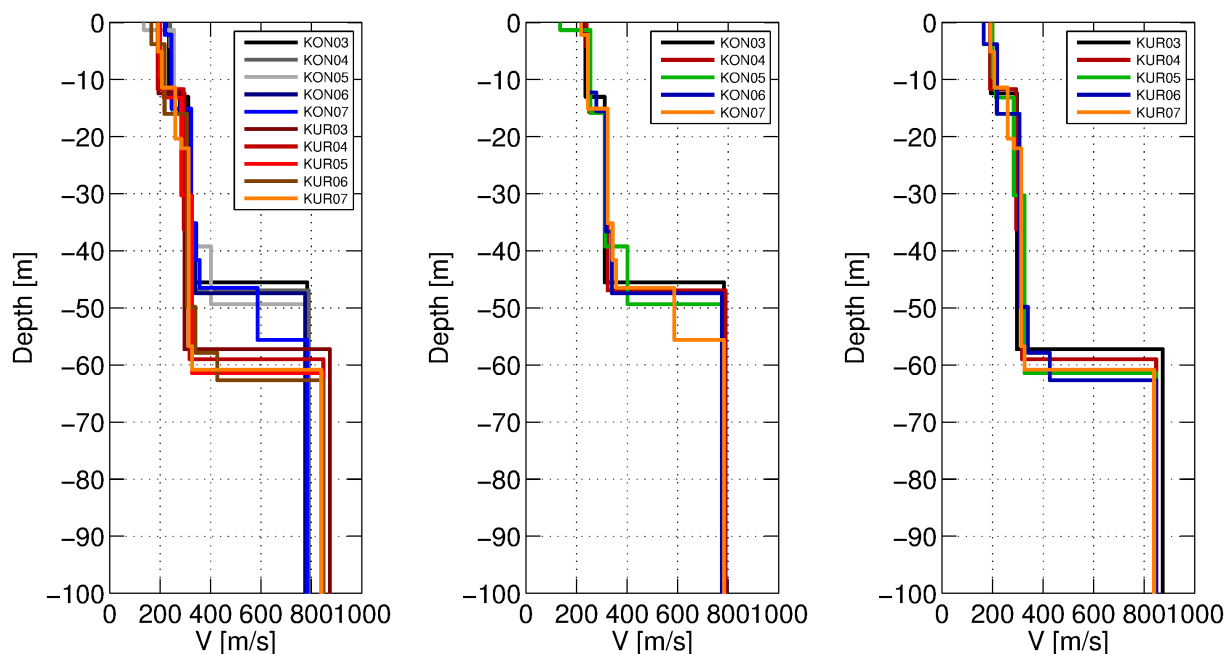

Figure 39: Overview of shear-wave velocity profiles of the best-fitting models of all inversions (left), for the KON inversions (center) and the KUR inversions (right).

6.3 SH transfer function

Although the empirical amplification for station SDAK is only based on three events so far, the fundamental peak frequency fits very well with the theoretical amplification for the underground models. The higher peaks of the SH transfer function cannot be well explained by the inverted models.
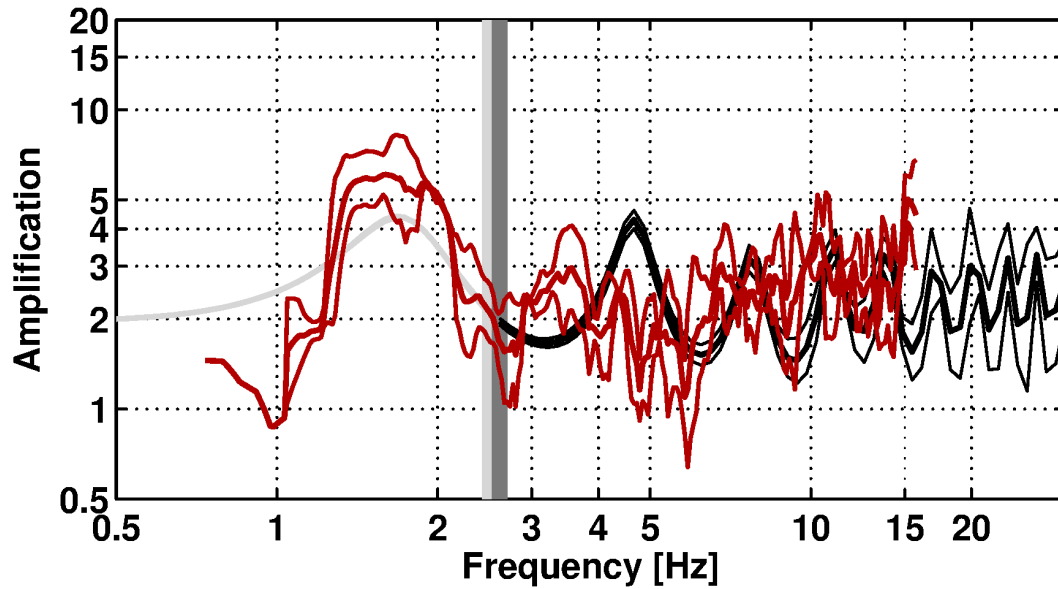

Figure 40: Comparison between the modeled amplification for the best models of the five different inversions of the KON array (black, with standard deviation) and the empirical amplification measured at station SDAK (red, with standard deviation).
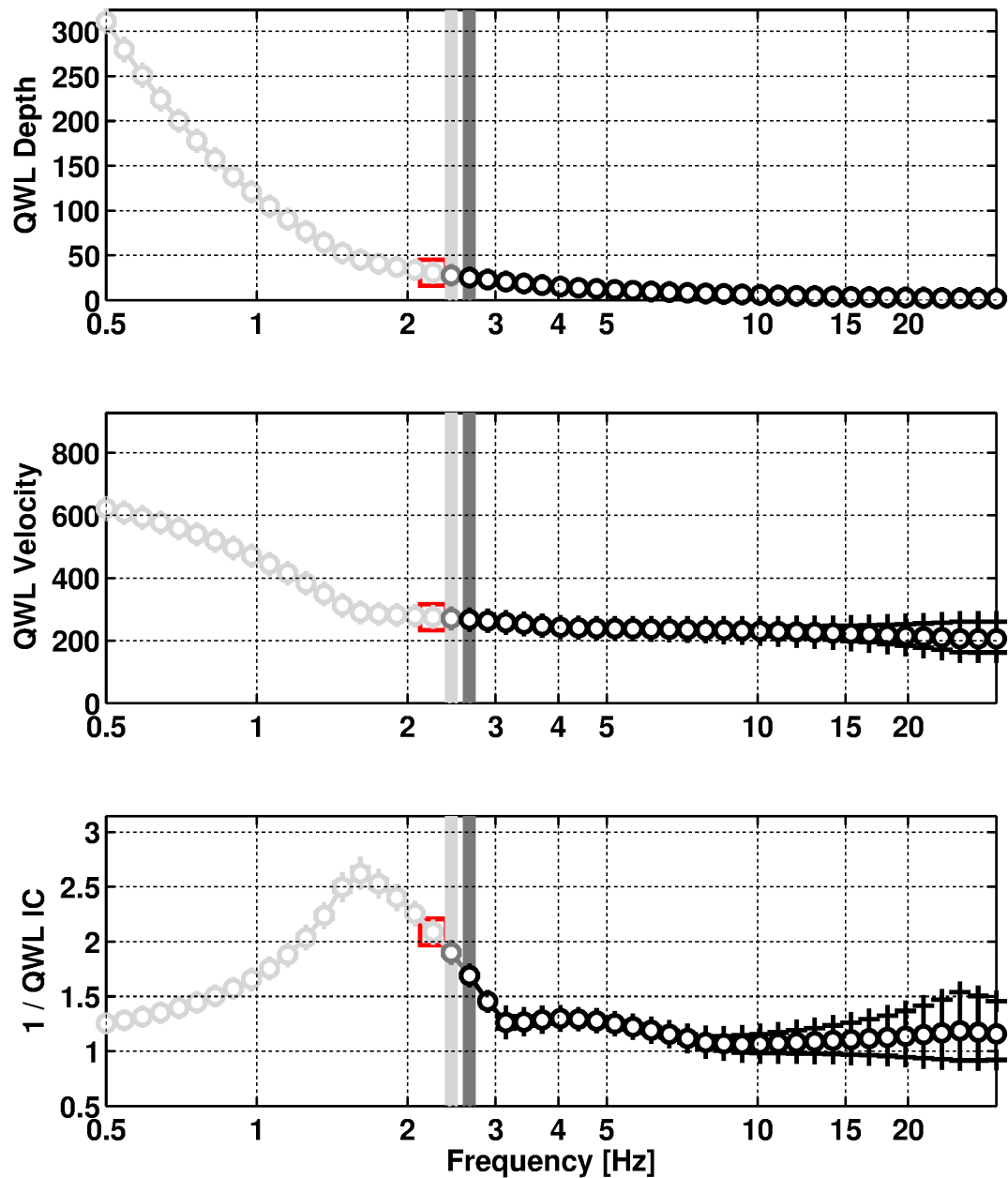
6.4 Quarter-wavelength representation

Figure 41: Quarter wavelength representation of the velocity profile for the best models of the five KON inversions (top: depth, center: velocity, bottom: inverse of the impedance contrast). The black curves are constrained by the dispersion curves, the light grey curves are not constrained by the data. The red square corresponds to V_{S30}.

7 Conclusion

We performed different measurements to characterize the underground under station SDAK in Davos, large-scale H/V measurements for the site selection and two array measurements (KON and KUR) in the vicinity of the station.

Our measurements show a 2-dimensional resonance of the valley at a frequency of about 1.1 Hz in the Kurpark and 1.25 Hz around the location of station SDAK. The ellipticity measurements at the different sites show ellipticity peaks at higher frequencies, around 1.5 Hz. The observed 2-dimensional resonance is not compatible with such ellipticity peaks and was therefore not further considered.

The different methods of array processing we used, namely 3-component HRFK, WaveDec and SPAC, gave coincident dispersion curves. In the Kurpark, the fundamental and first harmonic mode dispersion curves could be retrieved for both Love and Rayleigh waves. In the KON array, only the fundamental modes could be observed.

A joint inversion of the dispersion and ellipticity curves for the KUR and KON arrays showed that the most prominent features of the underground structure can be well described by a three-layered model (including the seismic bedrock). The inversion showed that the first layer is around 12 m thick at the KUR and KON sites and that the seismic bedrock is found at a depth of around 60 m in the Kurpark, which is in very good agreement with the contrast between the sedimentary layers and the underlying moraine which was found at a depth of 60 m by a borehole measurement in the Kurpark. Under the KON array, at the location of station SDAK, the bedrock depth is less than 50 m. The V_{S30} at this site is around 275 m/s.

Acknowledgements

References

Aki, K. (1957). Space and time spectra of stationary stochastic waves, with special reference to microtremors. *Bull. Earthquake Res. Inst. Tokyo Univ.*, 35:415–456.

Bard, P.-Y. and Bouchon, M. (1985). The two-dimensional resonance of sediment-filled valleys. *Bull. Seismol. Soc. Am.*, 75:519–541.

Bettig, B., Bard, P.-Y., Scherbaum, F., Riepl, J., Cotton, F., Cornou, C., and Hatzfeld, D. (2001). Analysis of dense array noise measurements using the modified spatial auto-correlation method (SPAC): application to the Grenoble area. *Boll. Geof. Teor. Appl.*, 42:281–304.

Burjánek, J., Gassner-Stamm, G., Poggi, V., Moore, J. R., and Fäh, D. (2010). Ambient vibration analysis of an unstable mountain slope. *Geophys. J. Int.*, 180:820–828.

Burjánek, J., Moore, J. R., Molina, F. X. Y., and Fäh, D. (2012). Instrumental evidence of normal mode rock slope vibration. *Geophys. J. Int.*, 188:559–569.

Fäh, D., Kind, F., and Giardini, D. (2001). A theoretical investigation of average H/V ratios. *Geophys. J. Int.*, 145:535–549.

Fäh, D., Wathelet, M., Kristekova, M., Havenith, H., Endrun, B., Stamm, G., Poggi, V., Burjanek, J., and Cornou, C. (2009). Using ellipticity information for site characterisation. NERIES deliverable JRA4 D4, available at http://www.neries-eu.org.

Hobiger, M., Bard, P.-Y., Cornou, C., and Le Bihan, N. (2009). Single station determination of Rayleigh wave ellipticity by using the random decrement technique (RayDec). *Geophys. Res. Lett.*, 36.

Maranò, S., Reller, C., Loeliger, H.-A., and Fäh, D. (2012). Seismic waves estimation and wavefield decomposition: Application to ambient vibrations. *Geophys. J. Int.*, 191:175–188.

McNamara, D. E. and Buland, R. P. (2004). Ambient noise levels in the continental United States. *Bull. Seismol. Soc. Am.*, 94:1517–1527.

Poggi, V. and Fäh, D. (2010). Estimating Rayleigh wave particle motion from three-component array analysis of ambient vibrations. *Geophys. J. Int.*, 180:251–267.

Regli, C., Kleboth, P., and Bolay, S. (2013). Geothermische Ressourcenanalyse im Bereich des Kongresszentrums; 2. und 3. Projektphase: Erkundungsbohrung, Bohrlochmessungen und -versuche - Schlussbericht. Technical Report G0939.3, GEOTEST.

Regli, C., Kleboth, P., and Krummenacher, B. (2010). Geothermische Ressourcenanalyse im Bereich des Kongresszentrums; 1. Projektphase: Seismische Untersuchungen - Schlussbericht. Technical Report G0939.2, GEOTEST.